



A Unified Microwave Radiative Transfer Model for General Planar Stratified Media: Slab Formulation

Journal:	<i>Transactions on Geoscience and Remote Sensing</i>
Manuscript ID:	TGRS-2012-00380.R1
Manuscript Type:	Regular paper
Date Submitted by the Author:	n/a
Complete List of Authors:	Tian, Miao; University of Colorado at Boulder, ECEE Gasiewski, Albin; University of Colorado at Boulder, Electrical and Computer Engineering
Keywords:	Remote sensing

SCHOLARONE™
Manuscripts

Review

1
2
3
4
5
6
7
8
9
10
11
12
13
14
15
16
17
18
19
20
21
22
23
24
25
26
27
28
29
30
31
32
33
34
35
36
37
38
39
40
41
42
43
44
45
46
47
48
49
50
51
52
53
54
55
56
57
58
59
60

1. Editor's Comments:

In order to increase the relevance of the paper for readers of the IEEE Trans. on Geoscience and Remote Sensing (TGRS), please add recent, related TGRS references (in particular from the years 2008 - 2011) where appropriate.

2. Associate Editor Comments to the Author:

The paper can be reconsidered for publication after minor revision as suggested by reviewer 1.

3. Reviewer 1:

- a) The main limitation of this work is that all the geophysical mediums are assumed to be moderately sized spherical scatters. However, ice and snow particles are well known to be non-spherical and therefore their phase functions are not symmetric. The authors should provide some error characterization about their assumptions.

Our answer: We realized that for a single particle using a spherical or non-spherical assumption will indeed yield significant brightness differences, and also realized that for certain non-spherical cases such as cylinders and spheroids, the associated scattering problems have been addressed (references can be listed if needed). The reason that we do not include the non-spherical cases in this work is that an intrinsic problem with non-spherical particle theory is that it will introduce more parameters, e.g., aspect ratios, orientation distributions, etc., into the problem. These parameters for non-spherical particles are difficult to actually measure, and if particles are randomly oriented in a medium the non-spherical and spherical cases usually give similar results in the polydispersed scattering case. We thus wanted to focus this modeling effort on the most basic of particle types and study the impact of other issues, such as polarization, refraction, discretization, integration accuracy, and fast Jacobian development.

- b) The authors also declared the UMRT has the rapid computation capability without giving evidence and comparison results with well-established models.

Our answer: Our discussion of rapid computation capability directly follows that for DOTLRT in the Section IX of Voronovich et al [2004]. In UMRT, the number of operations required for calculation of both the brightness temperature profile and associated Jacobian for all stream angles (M angles) is NM^3 , where N is the total number of layers. Since the same complexity applies we do not bother to belabor the discussion again.

As the previous argument goes: (1) for a conventional DOE solution with a divided difference Jacobian, the number of operations required is N^2 , and (2) for an iterative perturbation solution the number of operations is N^3 . Normally, $N \gg M$, therefore DOTLRT and UMRT are rapid models in this regard.

- c) Although the paper is well written and organized, I recommend it to be published only upon addressing the previous comments. I would also suggest that the number of equations be reduced significantly in the body of the paper as to make the publication reader-friendly.

1
2
3
4
5
6
7
8
9
10
11
12
13
14
15
16
17
18
19
20
21
22
23
24
25
26
27
28
29
30
31
32
33
34
35
36
37
38
39
40
41
42
43
44
45
46
47
48
49
50
51
52
53
54
55
56
57
58
59
60

Our response: we moved two parts: 1) the proof of positive definite matrix and 2) the solution procedure of the case using linear temperature profile to Appendix. At this moment, we tend to keep the both parts by considering the derivation integrity. However, these two parts can be removed if the reviewers and/or editors would like to.

Modification List:

1. In Abstract, the word “loosely” is replaced by “**tenuously**”
2. In Abstract, the word “both” is added: “...by including **both** the Mie theory and the dense media radiative transfer theory (DMRT).”
3. In Introduction, two paragraphs are added in order to response to Reviewer 1’s comments, starting with “During the development of UMRT...” to “...therefore DOTLRT and UMRT are rapid models in this regard.”
4. In Section II,
 - a) Eqn. (8) is removed, eqn. (9) is modified to reduce its length, and accordingly, some words are slightly modified to accommodate to the changes.
 - b) In Sec. II (D), “...between the Mie and DMRT-QCA theories...” is changed by “...between the DMRT-QCA and Mie theories...”
 - c) The subplot, Fig. 4(c), is corrected.
5. In Section III,
 - a) In sec. III (a), the proof of matrix $\bar{U} + \bar{D}$ being positive definite is move to Appendix I. The moved part begins with “In order to apply the stable matrix inversion...”, including eqns. (45-50).
 - b) In sec. III (b), the whole solution procedure for linear case starting with “Balancing...”, including eqns. (58-67), is moved to Appendix II.

A Unified Microwave Radiative Transfer Model for General Planar Stratified Media: Slab Formulation

Miao Tian, *Student Member, IEEE* and Albin J. Gasiewski, *Fellow, IEEE*

Abstract

A unified microwave radiative transfer model (UMRT) is presented for computing the thermal radiation emitted from any geophysical medium comprised of planar layers of either densely or tenuously distributed, moderately sized spherical scatterers. UMRT employs the discrete ordinate eigenanalysis method with layer-adding to solve the differential radiative transfer equation for such multilayer structures. UMRT inherits the symmetrization and analytical diagonalization and factorization techniques of symmetric and positive definite matrices from the discrete ordinate tangent linear radiative transfer model (DOTLRT) presented in Voronovich *et al.* [1]. These techniques ensure accuracy, numerical stability, and rapid computation for all matrix operations required for discrete ordinate eigenanalysis along with a fast Jacobian calculation for radiance assimilation purposes. UMRT extends the applicability of DOTLRT by including both the Mie theory and the dense media radiative transfer theory (DMRT). Other nontrivial extensions within UMRT are: 1) the vertical and horizontal radiation intensities are coupled within each layer by applying the reduced Mie or DMRT phase matrices, and 2) the physical temperature profile of a layer is allowed to be linear in height. Symmetry properties of both the reduced Mie and DMRT phase matrices are proved, and the associated scattering and absorption coefficients are compared and discussed. The UMRT slab formulation is validated by imposing energy conservation and numerical results for some nominal cases are produced and discussed.

Index Terms

Microwave remote sensing, dense media, layered media, DMRT, Mie, polarization, Jacobian, symmetric and positive definite matrix.

I. INTRODUCTION

Currently, a major challenge in passive microwave remote sensing is the accurate and fast forward numerical modeling of the electromagnetic scattering and emission properties of any geophysical media

M. Tian and A. J. Gasiewski are with the Center for Environmental Technology, Department of Electrical and Computer Engineering, University of Colorado, Boulder, CO 80309-0425 USA (email: Miao.Tian@Colorado.Edu or Albin.Gasiewski@Colorado.Edu).

1
2 consisting of soil, water, snow, ice, rain, cloud, fog, etc. Of importance in any such numerical model
3 is accuracy, numerical stability, computational speed, applicability to both dense and tenuous scattering
4 media, and the capability to produce a Jacobian for radiance assimilation purposes.
5
6
7

8 Three primary solution techniques to solve the differential radiative transfer equation (DRTE) for the four
9 Stokes parameters are: 1) the iterative method [2], [3], 2) the discrete ordinate eigenanalysis (DOE) method
10 [4]–[7], and 3) the Monte Carlo method [8], [9]. Among these, the iterative method is applicable to low
11 albedo cases or thin layers, and the Monte Carlo method lacks physical insight and convergence criteria.
12 The DOE method with layer-adding is widely used due to its applicability to layers of arbitrary albedo. In
13 the DOE method, the continuum of propagation directions is described by a finite number of quadrature
14 angles. The resulting system of equations is solved by eigenanalysis, and medium inhomogeneity is
15 accommodated by layer-adding.
16
17
18
19
20
21
22
23

24 The basic DOE solution for a multilayer structure under the planar stratified approximation follows the
25 formulation developed by Stamnes and Swanson [5]. In this work a matrix-operator method to solve the
26 DRTE as an eigenvalue problem and technique to reduce the order of the problem by a factor of two
27 were devised. In 1986, Nakajima and Tanaka [6] introduced the decomposition of a symmetric transition
28 matrix to provide a nearly-stable numerical solution for the DRTE. Matrix operator representations of
29 the reflection and transmission matrices in the multilayer stack were also introduced in their algorithm.
30 In 1988, the DOE model was summarized by Stamnes [7] for general use in planar multilayer multiple
31 scattering media.
32
33
34
35
36
37
38
39

40 Although the above models have been successful, there remained two major problems within the DOE
41 formulation: 1) analytic functions of matrices were required to be computed using Taylor series expansions.
42 For example, for a sufficiently small transition matrix argument $\overline{\overline{A}}\overline{\overline{B}}h$, one can calculate the cosine
43 hyperbolic operator of this argument as:
44
45
46
47
48
49

$$\cosh\left(\sqrt{\overline{\overline{A}}\overline{\overline{B}}}h\right) = 1 + \frac{\overline{\overline{A}}\overline{\overline{B}}}{2!}h^2 + \frac{\left(\overline{\overline{A}}\overline{\overline{B}}\right)^2}{4!}h^4 + \dots \quad (1)$$

50 The above expansion generally requires too many terms for practical implementation. Accordingly, the
51 accuracy of the DOE solution is compromised by accumulated roundoff errors. 2) A second issue is
52 the well-known matrix inversion instability associated with implementation of the DOE method for high
53 albedo, high opacity and thick layers. These two attributes have historically limited the applicability of
54
55
56
57
58
59
60

DOE method.

To circumvent these problems Voronovich *et al.* [1] developed the discrete ordinate tangent linear radiative transfer model (DOTLRT) based on symmetrization of the DRTE and analytical diagonalization and factorization of the resulting symmetric and positive definite matrices to provide inherent computational stability and high computational efficiency for all matrix operations required by the DOE method. The core DOTLRT procedure requires that both transition matrices $\overline{\overline{A}}$ and $\overline{\overline{B}}$ are symmetric and positive definite, in which case any arbitrary analytic function g operated on the matrix product $\overline{\overline{A}}\overline{\overline{B}}$ can be readily calculated. Specifically, applying symmetry the matrix $\overline{\overline{A}}$ can be represented as

$$\overline{\overline{A}} = \overline{\overline{M}}_1 \overline{\overline{\Lambda}}_1 \overline{\overline{M}}_1^T \quad (2)$$

where $\overline{\overline{M}}_1$ is an orthogonal matrix consisting of eigenvectors of $\overline{\overline{A}}$ having the following characteristics:

$$\overline{\overline{M}}_1 \overline{\overline{M}}_1^T = \overline{\overline{M}}_1 \overline{\overline{M}}_1^{-1} = \overline{\overline{I}} \quad (3)$$

where $(\cdot)^T$ denotes the matrix transpose and $\overline{\overline{I}}$ is the identity matrix. In (2), $\overline{\overline{\Lambda}}_1$ is a diagonal matrix of associated eigenvalues. Since $\overline{\overline{A}}$ is positive definite, the eigenvalues are positive ($\{\overline{\overline{\Lambda}}_1\}_{ii} > 0$), which guarantees that values of $\overline{\overline{\Lambda}}_1^{\pm\frac{1}{2}}$ are all positive real. Similarly, another set of eigenvalue and eigenvector matrices can be defined using the matrices $\overline{\overline{B}}$ and $(\overline{\overline{\Lambda}}_2, \overline{\overline{M}}_2)$ in (2) as

$$\overline{\overline{\Lambda}}_2^{-\frac{1}{2}} \overline{\overline{M}}_2^T \overline{\overline{B}} \overline{\overline{M}}_2 \overline{\overline{\Lambda}}_2^{\frac{1}{2}} = \overline{\overline{M}}_2 \overline{\overline{\Lambda}}_2 \overline{\overline{M}}_2^T \quad (4)$$

Using (2) and (4), the product of $\overline{\overline{A}}\overline{\overline{B}}$ can be calculated as

$$\overline{\overline{A}}\overline{\overline{B}} = \left(\overline{\overline{M}}_1 \overline{\overline{\Lambda}}_1^{\frac{1}{2}} \overline{\overline{M}}_2 \right) \overline{\overline{\Lambda}}_2 \left(\overline{\overline{M}}_1 \overline{\overline{\Lambda}}_1^{-\frac{1}{2}} \overline{\overline{M}}_2 \right)^T \quad (5)$$

As a result,

$$g\left(\overline{\overline{A}}\overline{\overline{B}}\right) = \left(\overline{\overline{M}}_1 \overline{\overline{\Lambda}}_1^{\frac{1}{2}} \overline{\overline{M}}_2 \right) g\left(\overline{\overline{\Lambda}}_2\right) \left(\overline{\overline{M}}_1 \overline{\overline{\Lambda}}_1^{-\frac{1}{2}} \overline{\overline{M}}_2 \right)^T \quad (6)$$

for any matrix function g . Moreover, by incorporating the derivative chain rule using first-order perturbations of the eigenvalues and eigenvectors of a symmetric matrix, DOTLRT provides rapid

1
2 numerical calculation of the associated Jacobians between the observed brightness temperature and all
3 relevant radiative parameters.
4

5
6 Although the DOTLRT algorithm provides a stable, fast and accurate solution to the DRTE, it was
7 originally developed for atmospheric simulation in which scattering hydrometeors are sparse (e.g., rain,
8 fog, cloud, and aerosols). It also is based on a single polarization using the Henyey-Greenstein (HG) phase
9 matrix approximation for a planar multilayer structure with non-refracting layers. Finally, it is based on
10 layers with constant physical temperature. These attributes have limited its application, especially for cases
11 of dense media (e.g., snow, ice, soil, etc.,) and thick atmospheric or surface layers with strong temperature
12 gradients.
13
14
15
16
17
18
19

20 In this paper, we present a new “unified microwave radiative transfer model” (UMRT) to extend
21 DOTLRT in all of the above areas. This model can be applied to widely varying types of media for
22 both forward radiative transfer and radiance assimilation purposes. Within UMRT we seamlessly partition
23 media layers into two categories, which are treated distinctively as follows: 1) sparse medium layers, in
24 which scatters are loosely distributed and independent scattering is dominant, and 2) dense medium layers,
25 in which scatters occupy significant volume fraction and volumetric scattering is dominant. For sparse
26 medium layers, the cross-polarization is considered by using the reduced Mie phase matrix. A proof of
27 the symmetry and positive definite nature of the Mie phase matrix is developed to ensure the applicability
28 of the stable matrix operation formulation of DOTLRT. Assuming independent scattering, UMRT sparse
29 medium layers are parametrized by sets of particle size distribution functions for each of the different
30 scatterer phases, for example, liquid spheres, ice spheres, etc. Calculations of the associated extinction,
31 scattering and absorption coefficients, and phase matrices are performed for each of these phases.
32
33
34
35
36
37
38
39
40
41
42
43

44 For dense medium layers, the dense media radiative transfer theory (DMRT) is applied within UMRT.
45 The DMRT theory with the quasi-crystalline approximation (QCA) was developed by Tsang and his
46 colleagues beginning in the early 1980s [8], [10]. In UMRT, a recent (2007) version of the DMRT-QCA
47 model by Tsang *et al.* [11] is used. This model uses a sticky particle assumption for moderately sized
48 (i.e., Mie-scale) spherical particles. In this model, the adhesion and aggregation of the sticky particles
49 are simulated by using sticky pair distribution functions based on the Percus-Yevick approximation. As
50 used within UMRT the reduced DMRT-QCA phase matrix is included and its symmetry properties are
51 identified. The associated absorption and scattering coefficients are calculated under the DMRT framework.
52
53
54
55
56
57
58
59

60 Other nontrivial extensions to DOTLRT incorporated within UMRT include extending the accuracy of

1 the single-layer DRTE solution by permitting the temperature profile to be linear in height. UMRT also
2 inherits from DOTLRT the capability for rapid Jacobian calculation for a general medium model.
3

4
5
6
7 During the development of UMRT, we realized that for a single particle using a spherical or non-
8 spherical assumption will indeed yield significant brightness differences, and also realized that for
9 certain non-spherical cases such as cylinders and spheroids, the associated scattering problems have been
10 addressed [4]. The reason we do not include the non-spherical cases in this work is that an intrinsic problem
11 with non-spherical particle theory is that it will introduce more parameters, e.g., aspect ratios, orientation
12 distributions, etc., into the problem. However, these parameters for non-spherical particles are difficult to
13 actually measure, and if particles are randomly oriented in a medium the non-spherical and spherical cases
14 usually give similar results in the polydispersed scattering case. We thus wanted to focus this modeling
15 effort on the most basic particle type and study the impact of other issues, such as polarization, refraction,
16 discretization, integration accuracy, computation speed and fast Jacobian development.
17
18
19
20
21
22
23
24
25
26

27
28 Our discussion of rapid computation capability directly follows that for DOTLRT in the Section IX of
29 [1]. In UMRT, the number of operations required for calculation of both the brightness temperature profile
30 and associated Jacobian for all stream angles (M angles) is NM^3 , where N is the total number of layers.
31 Since the same complexity applies we do not bother to belabor the discussion again. As the previous
32 argument goes: 1) for a conventional DOE solution with a divided difference Jacobian, the number of
33 operations required is N^2 , and 2) for an iterative perturbation solution the number of operations is N^3 .
34 Normally, $N \gg M$, therefore DOTLRT and UMRT are rapid models in this regard.
35
36
37
38
39
40
41

42 This paper focuses on the details of the UMRT formulation for a multilayer stack with non-refractive
43 boundaries. This paper is organized as follows: Section II summarizes the equations for the scattering
44 and absorption coefficients and phase matrices based on the Mie theory and the DMRT-QCA theory.
45 Proof of the symmetry property of both the Mie and DMRT-QCA phase matrices is included along with a
46 comparison of the two phase matrices. Section III provides the theoretical framework for UMRT, including
47 the DRTE symmetrization, the DOE solution to a single medium layer by using the decomposition of
48 symmetric and positive definite matrix and under the linear profile assumption, and the upward recursive
49 DOE solution to the multilayer stack with non-refractive boundaries. Section IV provides a validation of
50 the UMRT solution by imposing energy conservation and also presents numerical results for some nominal
51 environmental scenarios. Section V provides a brief conclusion and discussion of related ongoing work.
52
53
54
55
56
57
58
59
60

II. EXTINCTION, SCATTERING AND PHASE MATRICES

All numerical integrations in UMRT are computed by applying the Gauss-Legendre quadrature with the Christoffel weights [12], although in principal any quadrature scheme can be implemented. It is nontrivial to point out that UMRT employs the method derived by Yakimiw [12] to compute the Gauss-Legendre nodes and weights. According to [13], the Yakimiw method reduces both the error growth in the nodes and weights computations from the orders $O(n)$ and $O(n^2)$ of the eigensystem method to $O(1)$ and $O(n)$, respectively. Moreover, the Yakimiw method is suitable in terms of accuracy, reliability and speed for computing the nodes and weights of very high order Gauss quadrature rules with $n \sim 10^4$, which are currently used for high resolution global atmospheric models.

A. Stokes Matrix: Transformation and Symmetry

In radiative transfer theory, the relationship between the incident and scattered Stokes vectors, $\bar{I}_i(\Theta)$ and $\bar{I}_s(\Theta)$, respectively, for a single particle is depicted in the particle-based system of coordinates (Fig. 1(a)) and described by

$$\bar{I}_s(\Theta) = \frac{1}{r^2} \bar{\bar{L}}(\Theta) \cdot \bar{I}_i(\Theta) \quad (7)$$

where $\bar{\bar{L}}(\Theta)$ is the Stokes matrix for a single particle and has the following simplified form due to the symmetry of spherical particles [4].

$$\bar{\bar{L}}(\Theta) = \begin{bmatrix} |f_{11}|^2 & 0 & 0 & 0 \\ 0 & |f_{22}|^2 & 0 & 0 \\ 0 & 0 & \text{Re}\{f_{11}f_{22}^*\} & -\text{Im}\{f_{11}f_{22}^*\} \\ 0 & 0 & \text{Im}\{f_{11}f_{22}^*\} & \text{Re}\{f_{11}f_{22}^*\} \end{bmatrix} \quad (8)$$

where $f_{\alpha\beta}$, $\alpha, \beta = 1$ or 2 is the scattering amplitude and represents the scattering between polarizations.

Although the particle-based system has advantages in providing simple forms of the scattering amplitudes for particles with symmetry, it is necessary for modeling stratified media to express the scattering amplitudes in the principal coordinate system, defined by the scattering and incident angles $(\theta_s, \phi_s; \theta_i, \phi_i)$ [4], [14], [15], shown in Fig. 1(b).

The transformation between the two coordinate systems is given by

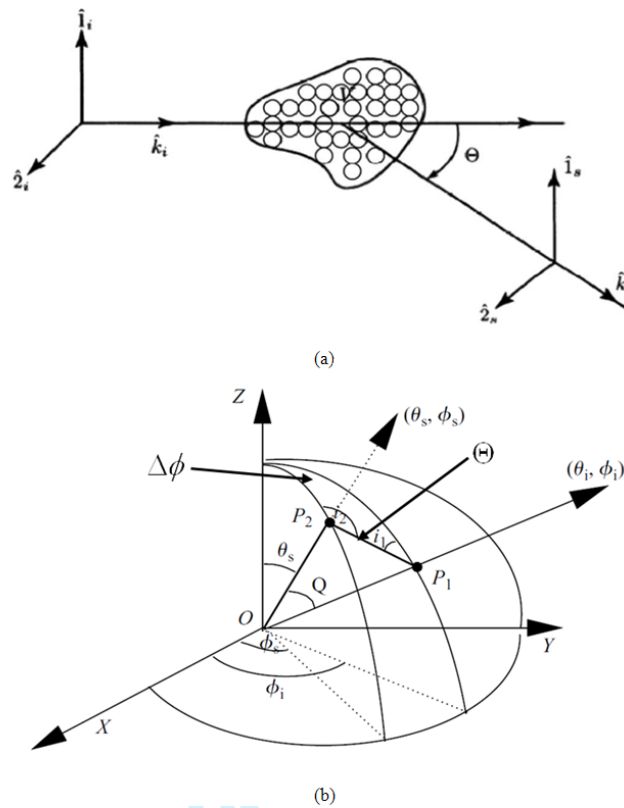


Figure 1. (a) Particle-based coordinate system (from [4]) defined by scattering plane containing \hat{k}_i and \hat{k}_s , which are the incident and scattered directions, respectively. The angle between \hat{k}_i and \hat{k}_s is Θ . (b) principal coordinate system defined by $(\theta_s, \phi_s; \theta_i, \phi_i)$ and the relationship between the two coordinate systems (from [15]).

$$\bar{\bar{L}}(\theta_s, \phi_s; \theta_i, \phi_i) = \bar{\bar{L}}_r(-i_2) \bar{\bar{L}}(\Theta) \bar{\bar{L}}_r(-i_1) \quad (9)$$

where $\bar{\bar{L}}_r$ is the rotation matrix [14], [16]

$$\bar{\bar{L}}_r(i_{1,2}) = \begin{bmatrix} \cos^2 i_{1,2} & \sin^2 i_{1,2} & 0.5 \sin 2i_{1,2} & 0 \\ \sin^2 i_{1,2} & \cos^2 i_{1,2} & -0.5 \sin 2i_{1,2} & 0 \\ -\sin 2i_{1,2} & \sin 2i_{1,2} & \cos 2i_{1,2} & 0 \\ 0 & 0 & 0 & 1 \end{bmatrix} \quad (10)$$

and the angles i_1 and i_2 are each spherical surface angles. From [15], the cosine of these two angles are expressed as

$$\cos i_1 = \frac{\cos \theta_s \sin \theta_i - \cos \theta_i \sin \theta_s \cos \Delta \phi}{\sin \Theta} \quad (11)$$

$$\cos i_2 = \frac{\cos \theta_i \sin \theta_s - \cos \theta_s \sin \theta_i \cos \Delta \phi}{\sin \Theta} \quad (12)$$

where

$$\begin{aligned}\Delta\phi &= \phi_i - \phi_s \\ \sin\Theta &= \sqrt{1 - \cos^2\Theta} \\ \cos\Theta &= \cos\theta_s\cos\theta_i + \sin\theta_s\sin\theta_i\cos\Delta\phi\end{aligned}$$

The spherical surface angles i_1 and i_2 can be computed by following equations without ambiguity:

$$i_{1,2} = \begin{cases} 2\pi - \arccos[\cos(i_{1,2})], & \pi < \Delta\phi < 2\pi \\ \arccos[\cos(i_{1,2})], & 0 < \Delta\phi < \pi \end{cases} \quad (13)$$

In general, $\bar{\bar{L}}(\theta_s, \phi_s; \theta_i, \phi_i)$ is a full 4×4 matrix whereas $\bar{\bar{L}}(\Theta)$ has only six nonzero elements, four of which are independent.

The analytical diagonalization and factorization technique used within UMRT requires symmetry of the phase (and thus Stokes) matrix in the principal coordinate system under scattering path reversal (i.e., $\theta_s \leftrightarrow \theta_i$). To show this degree of symmetry, the following equalities are examined by applying the coordinate transformation defined within (9-13):

$$\begin{aligned}\bar{\bar{L}}(\theta_s, \theta_i; \Delta\phi) &\stackrel{?}{=} [\bar{\bar{L}}(\theta_i, \theta_s; \Delta\phi)]^T \\ \bar{\bar{L}}(\theta_s, \pi - \theta_i; \Delta\phi) &\stackrel{?}{=} [\bar{\bar{L}}(\theta_i, \pi - \theta_s; \Delta\phi)]^T\end{aligned} \quad (14)$$

for which they would (respectively) follow that:

$$\begin{aligned}\bar{\bar{L}}_r(-i_2)\bar{\bar{L}}(\Theta)\bar{\bar{L}}_r(-i_1) &\stackrel{?}{=} [\bar{\bar{L}}_r(-i_1)\bar{\bar{L}}(\Theta)\bar{\bar{L}}_r(-i_2)]^T \\ \bar{\bar{L}}_r(-i_1)\bar{\bar{L}}(\Theta)\bar{\bar{L}}_r(-i_2) &\stackrel{?}{=} [\bar{\bar{L}}_r(i_2)\bar{\bar{L}}(\Theta)\bar{\bar{L}}_r(i_1)]^T\end{aligned} \quad (15)$$

Applying a Stokes matrix $\bar{\bar{L}}(\Theta)$ for a spherical particle with form as in (8) to (15) the equalities in (14-15) hold for the diagonal and $v - h$ elements, viz:

$$\bar{\bar{\Delta}} = \begin{bmatrix} 0 & 0 & \Delta_{13} & \Delta_{14} \\ 0 & 0 & \Delta_{23} & \Delta_{24} \\ \Delta_{31} & \Delta_{32} & 0 & \Delta_{34} \\ \Delta_{41} & \Delta_{42} & \Delta_{43} & 0 \end{bmatrix} \quad (16)$$

where $\overline{\overline{\Delta}} \triangleq \overline{\overline{L}}(\theta_s, \theta_i; \Delta\phi) - \left[\overline{\overline{L}}(\theta_i, \theta_s; \Delta\phi) \right]^T$ or $\overline{\overline{L}}(\theta_s, \pi - \theta_i; \Delta\phi) - \left[\overline{\overline{L}}(\theta_i, \pi - \theta_s; \Delta\phi) \right]^T$ and Δ_{ij} represents a non-zero matrix element. Eq. (16) shows that the Stokes matrix $\overline{\overline{L}}(\theta_s, \theta_i; \Delta\phi)$ for spheres is symmetric for the first two Stokes parameters. More specifically, if $\overline{\overline{L}}(\Theta)$ is calculated from either the Mie or DMRT scattering theory, the difference matrix $\overline{\overline{\Delta}}$ is found by numerical calculation for a wide range of parameters and angles comprising nearly one million diverse cases to be:

$$\overline{\overline{\Delta}} = \begin{bmatrix} \sim 0 & \sim 0 & \sim 0 & \sim 0 \\ \sim 0 & \sim 0 & \sim 0 & \sim 0 \\ \sim 0 & \sim 0 & \sim 0 & \Delta_{34} \\ \sim 0 & \sim 0 & \Delta_{43} & \sim 0 \end{bmatrix} \quad (17)$$

where the ' ~ 0 ' entries are zero within standard IEEE numerical precision. While not an absolute proof the above strongly suggests that both the Mie and DMRT Stokes matrices are symmetric for the first three Stokes parameters.

Moreover, if the Stokes matrix $\overline{\overline{L}}(\Theta)$ has the simplified form of the Rayleigh Stokes matrix (i.e., for electrically small particles):

$$\overline{\overline{L}}(\Theta) = \frac{3}{2} \begin{bmatrix} \cos^2 \Theta & 0 & 0 & 0 \\ 0 & 1 & 0 & 0 \\ 0 & 0 & \cos \Theta & 0 \\ 0 & 0 & 0 & \cos \Theta \end{bmatrix} \quad (18)$$

Then it can be shown that $\overline{\overline{\Delta}} = \overline{\overline{0}}$ for all entries. Hence, in this case of small particles $\overline{\overline{L}}(\theta_s, \theta_i; \Delta\phi)$ is symmetric for all four Stokes parameters.

B. Mie Phase Matrix

From [2], [4], the phase matrix is calculated by integrating the Stokes matrix with respect to an appropriate particle size distribution function, $n(D)$.

$$\overline{\overline{P}}(\theta_s, \theta_i; \Delta\phi) = \int_0^\infty \overline{\overline{L}}(\theta_s, \theta_i; \Delta\phi) \cdot n(D) dD \quad (19)$$

where D is the sphere diameter. The details of various $n(D)$ functions relevant for atmospheric hydrometeors can be found in [2].

Due to the azimuthal symmetry of the planar-stratified media model employed in UMRT the phase matrix can be further simplified by dimensional reduction to a reduced phase matrix [2]:

$$\overline{\overline{P}}'(\theta_s, \theta_i) \equiv \int_0^{2\pi} \overline{\overline{P}}(\theta_s, \theta_i; \Delta\phi) d(\Delta\phi) \quad (20)$$

The reduced phase matrix is only a function of the incident angle θ_i and scattered angle θ_s . Due to the azimuthal symmetry within the Mie and DMRT theories it can be shown that the reduced phase matrix becomes:

$$\overline{\overline{P}}'(\theta_s, \theta_i)_{\text{Mie/DMRT}} = \begin{bmatrix} P_{11} & P_{12} & 0 & 0 \\ P_{21} & P_{22} & 0 & 0 \\ 0 & 0 & P_{33} & P_{34} \\ 0 & 0 & P_{43} & P_{44} \end{bmatrix} \quad (21)$$

where it is seen that the 1st and 2nd Stokes parameters are decoupled from the 3rd and 4th.

The equations related to the Mie phase matrix are summarized by noting the scattering amplitudes from the Mie theory [17], [18] are:

$$\begin{aligned} f_{11}(\Theta) &= \frac{-j}{k} \sum_{n=1}^{n_{max}} \frac{2n+1}{n(n+1)} [a_n \pi_n(\cos\Theta) + b_n \tau_n(\cos\Theta)] \\ f_{22}(\Theta) &= \frac{-j}{k} \sum_{n=1}^{n_{max}} \frac{2n+1}{n(n+1)} [a_n \tau_n(\cos\Theta) + b_n \pi_n(\cos\Theta)] \end{aligned} \quad (22)$$

where k is the wavenumber in air, (a_n, b_n) are the Mie scattering coefficients, and (π_n, τ_n) are the angle-dependent functions. The choice of maximum iteration number is commonly determined by $n_{max} = \text{round}(x + 4x^{\frac{1}{3}} + 2)$, where $x = ka$ is the size parameter, a is the sphere radius and the operation, $\text{round}(\cdot)$ returns the closest integer less than (\cdot) . Accordingly, the Mie phase matrix elements for a specific particle size distribution function $n(D)$ are computed as:

$$\begin{aligned} P_{11}(\Theta) &= \int_0^\infty |f_{11}(\Theta)|^2 \cdot n(D) dD \\ P_{22}(\Theta) &= \int_0^\infty |f_{22}(\Theta)|^2 \cdot n(D) dD \\ P_{33}(\Theta) &= \int_0^\infty \text{Re}\{f_{11}(\Theta) \cdot f_{22}^*(\Theta)\} \cdot n(D) dD \\ P_{44}(\Theta) &= P_{33}(\Theta) \end{aligned}$$

$$\begin{aligned}
 P_{34}(\Theta) &= -\int_0^\infty \text{Im}\{f_{11}(\Theta) \cdot f_{22}^*(\Theta)\} \cdot n(D) dD \\
 P_{43}(\Theta) &= -P_{34}(\Theta)
 \end{aligned} \tag{23}$$

In computing the reduced Mie phase matrix elements it is usually convenient to integrate the above expressions numerically with respect to the azimuthal angle as in (20). It is also convenient to define the reduced normalized phase matrix [2]:

$$\overline{\overline{P}}'(\theta_s, \theta_i) \equiv \frac{\overline{\overline{P}}'(\theta_s, \theta_i)}{\kappa_s} \tag{24}$$

where $\int_0^\pi \overline{\overline{P}}'(\theta_s, \theta_i) \sin \theta_s d\theta_s = 1$.

Within UMRT, for sparse media the extinction and scattering coefficients κ_e and κ_s are calculated based on the Mie theory for polydispersed particles [2] while for dense media they are calculated differently under the DMRT-QCA theory (c.f. §2.3). Using Mie theory the efficiencies η_e and η_s for monodispersed spherical particles are computed as

$$\begin{aligned}
 \eta_e &= \frac{2}{x^2} \sum_{n=1}^{n_{max}} (2n+1) \text{Re}(a_n + b_n) \\
 \eta_s &= \frac{2}{x^2} \sum_{n=1}^{n_{max}} (2n+1) (|a_n|^2 + |b_n|^2)
 \end{aligned} \tag{25}$$

Given a size distribution function $n(D)$ the coefficients for polydispersed spherical particles are computed as

$$\begin{aligned}
 \kappa_e &= \frac{\pi}{4} \int_0^\infty \eta_e \cdot D^2 \cdot n(D) dD \\
 \kappa_s &= \frac{\pi}{4} \int_0^\infty \eta_s \cdot D^2 \cdot n(D) dD
 \end{aligned} \tag{26}$$

As in [2] the upper limit of the above integrations are set to be 15 times the mean particle diameter $\langle D \rangle$. Since $n(D)$ is typically an exponential function, integrand contributions typically diminish after a few mean diameters.

C. DMRT-QCA Phase Matrix

UMRT employs the DMRT-QCA model outlined in [11], which simplifies the calculation of the DMRT-QCA phase matrix relative to previous implementations. The effective propagation constant K and the average multipole amplitudes $X_v^{(M)}$ and $X_v^{(N)}$ are numerically calculated by solving the $2N_{max}$ system

of equations obtained using the Lorentz-Lorentz (L-L) law and the Ewald-Oseen extinction theorem. The above quantities are subsequently used to calculate the DMRT-QCA Stokes matrix elements:

$$\begin{aligned}
 f_{11}(\Theta) &= \frac{-j}{(1-R)} \sqrt{\frac{1}{kK_r}} \sum_{n=1}^{N_{max}} \frac{2n+1}{n(n+1)} \\
 &\quad \times \left[a_n X_n^{(N)} \pi_n(\cos\Theta) + b_n X_n^{(M)} \tau_n(\cos\Theta) \right] \\
 f_{22}(\Theta) &= \frac{-j}{(1-R)} \sqrt{\frac{1}{kK_r}} \sum_{n=1}^{N_{max}} \frac{2n+1}{n(n+1)} \\
 &\quad \times \left[a_n X_n^{(N)} \tau_n(\cos\Theta) + b_n X_n^{(M)} \pi_n(\cos\Theta) \right]
 \end{aligned} \tag{27}$$

where k is the wavenumber in air, $K_r = \text{Re}\{K\}$, and R is a coefficient

$$R = \frac{-j\pi n_o}{k^2(k+K_r)} \sum_{n=1}^{N_{max}} (-1)^n [b_n X_n^{(M)} - a_n X_n^{(N)}] (2n+1) \tag{28}$$

The phase matrix elements are:

$$\begin{aligned}
 P_{11}(\Theta) &= |f_{11}(\Theta)|^2 q(\Theta) \\
 P_{22}(\Theta) &= |f_{22}(\Theta)|^2 q(\Theta) \\
 P_{33}(\Theta) &= P_{44}(\Theta) = \text{Re}\{f_{11}(\Theta) \cdot f_{22}^*(\Theta)\} q(\Theta) \\
 P_{34}(\Theta) &= -P_{43}(\Theta) = -\text{Im}\{f_{11}(\Theta) \cdot f_{22}^*(\Theta)\} q(\Theta)
 \end{aligned} \tag{29}$$

where the factor $q(\Theta)$ is obtained using the Percus-Yevick (PY) approximation in ([11], eqs. 10-11). In DMRT-QCA, the scattering and absorption coefficients are computed as follows:

$$\begin{aligned}
 \kappa_a &= \frac{k}{K_r} \frac{2\pi}{k^2 |1-R|^2} n_o \cdot \sum_{n=1}^{N_{max}} (2n+1) \left[|X_n^{(M)}|^2 \right. \\
 &\quad \left. (\text{Re}\{b_n\} - |b_n|^2) + |X_n^{(N)}|^2 (\text{Re}\{a_n\} - |a_n|^2) \right] \\
 \kappa_s &= \pi \int_0^\infty [P_{11}(\Theta) + P_{22}(\Theta)] \sin\Theta d\Theta \\
 \kappa_e &= \kappa_a + \kappa_s
 \end{aligned} \tag{30}$$

D. Results and Discussion

Comparisons of the scattering and absorption coefficients from the Mie theory and the DMRT-QCA theory as functions of frequency for several typical conditions illustrate fundamental differences between these distinct models (Tab. I and Fig. 2).

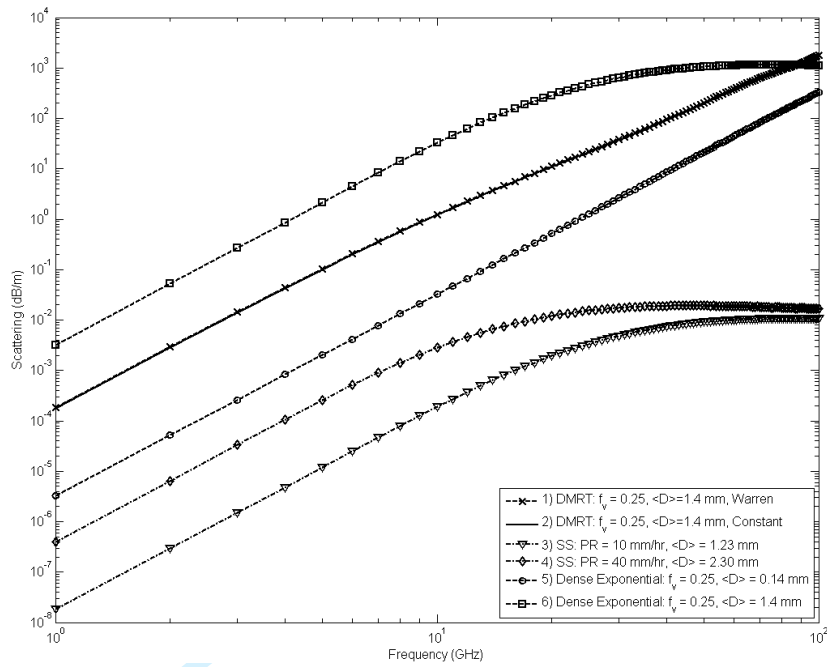
Table I

CONDITIONS FOR CALCULATING SCATTERING AND ABSORPTION COEFFICIENTS FOR VARIOUS ICE PARTICLE DISTRIBUTIONS AND FOR (1-2) DMRT-QCA THEORY, AND (3-6) MIE THEORY, FOR WHICH CASES 3-4 USE SPARSE SEKHON-SRIVASTAVA (SS) ICE SIZE DISTRIBUTIONS FOR TWO NOMINAL PRECIPITATION RATES WHILE 5-6 USE DENSE EXPONENTIAL SIZE DISTRIBUTIONS FOR A FIXED VOLUME FRACTION AND TWO PARTICLE DIAMETERS.

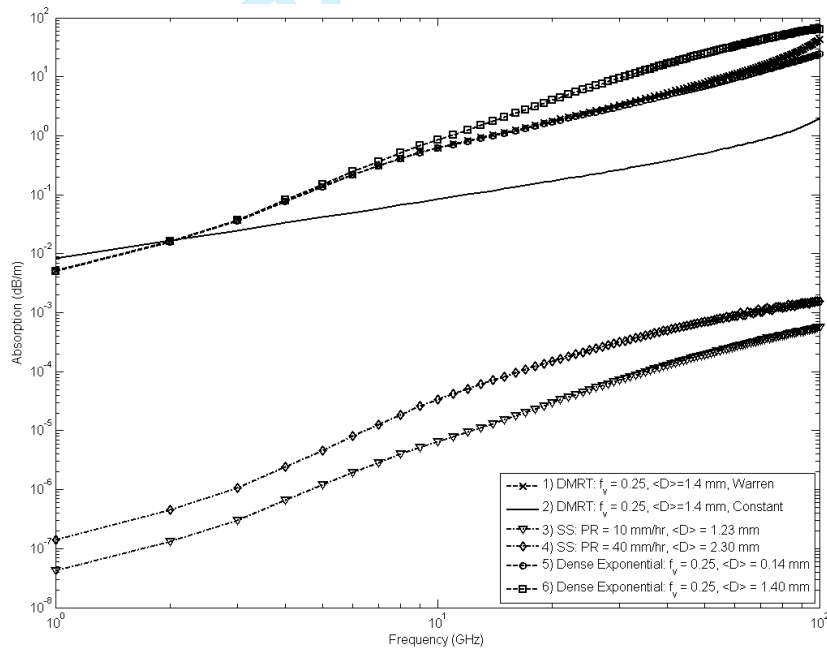
	f_v	n_o ($\text{m}^{-3} \text{mm}^{-1}$)	$\langle D \rangle$ (mm)
1) DMRT-QCA	2.5×10^{-1}	1.74×10^2	1.40
2) DMRT-QCA	2.5×10^{-1}	1.74×10^2	1.40
3) Mie, SS (PR = 10 mm/hr)	7.33×10^{-7}	2.87×10^2	1.23
4) Mie, SS (PR = 40 mm/hr)	1.07×10^{-7}	7.80×10^1	2.30
5) Mie, Dense exponential	2.5×10^{-1}	2.07×10^7	0.14
6) Mie, Dense exponential	2.5×10^{-1}	2.07×10^3	1.40

For purposes of comparison cases 2-6 use the fixed lossy value of ice permittivity of $\epsilon_{ice} = 3.15 - j0.001$, while case 1 uses the frequency dependent value obtained from [19].

The differences in both κ_s and κ_a between the DMRT-QCA and Mie theories for identical ice volume fractions are seen in cases 1-2 and 5-6 of Fig. 2(a-b), where DMRT-QCA generally predicts smaller values for κ_s than the Mie theory for the same mean particle sizes and overall densities (cases 1-2 and 6). However, since absorption is more closely related to the internal field amplitude and particle volume the differences are smaller than for scattering. This effect is seen more clearly by considering cases 5-6, where the mean particle size of the Mie simulation is varied by a factor of 10. For these cases the scattering coefficient for Rayleigh-sized particles increases by $\langle D \rangle^6 / n_o$, but there is less effect on the absorption coefficient, especially for the frequencies less than 10 GHz. In Fig. 2(a), we also note that κ_s of Mie theory saturates with larger particles at higher frequencies. This behavior suggests that the Mie scattering coefficient has a weaker frequency dependence than that of DMRT-QCA. As can be expected, Fig. 2(a) and 2(b) also show that the values of both κ_s and κ_a under Mie scattering for a dense distribution (cases 5-6) are much greater than their corresponding counterparts determined using the sparse Sekhon-Srivastava (SS, [20]) distribution (cases 3-4). This difference is the result of scaling by the volume fraction, and is inherent in Mie theory. However, the DMRT-QCA scattering coefficient depends non-linearly on f_v , and is accurately computable to volume fractions of at least $\sim 20\%$ [9]. Finally, in cases 1-2 it is noted that use of the nominal value for the ice dielectric constant in computing the value of κ_s does not result in obvious differences when compared with results using the ice dielectric constant values from Warren [19], however, these two dielectric constant models do result in significant differences in the value of κ_a . Accordingly, improved models of the dielectric constant of homogeneous water ice are suggested to be of interest.



(a) Scattering Coefficients



(b) Absorption Coefficients

Figure 2. (a) Scattering and (b) absorption coefficients for polydisperse ice particles computed using Mie and DMRT-QCA theories.

The behavior of reduced normalized Mie phase matrices are studied by assuming a rain case with the following conditions: 1) Marshall-Palmer (MP) size distribution [21] with precipitation rate = 10 mm/hr and 2) mean drop diameter $\langle D \rangle = 2$ mm. The water dielectric constant is determined using the double Debye model [22] at a temperature of 0°C. As seen in Fig. 3(a-c), the reduced normalized Mie phase matrices exhibit the expected symmetry for both vertical and horizontal polarizations. The plots further

1 show that forward scattering relative to back- or side-scattering increases as frequency increases, gradually
 2 becoming dominant above ~ 100 GHz as suggested by calculations of polydispersive asymmetry in [2].
 3

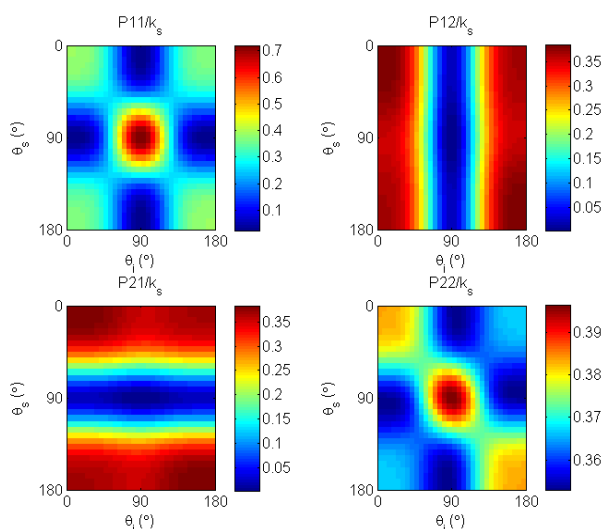
4 Analogously, Fig. 4 shows the reduced normalized DMRT-QCA phase matrices computed for a dense
 5 snowpack under the following conditions: 1) dielectric constant of ice of $\epsilon_{ice} = 3.15 - j0.001$, 2) mean ice
 6 diameter of $\langle D \rangle = 1.4$ mm, 3) volume fraction $f_v = 25\%$, 4) stickiness parameter $\tau = 0.1$. As shown, the
 7 reduced DMRT-QCA phase matrices also exhibit the expected symmetry as found for the Mie case, and
 8 the forward scattering also increases as frequency increases. Moreover, the DMRT-QCA phase matrices
 9 present more forward scattering than that of the comparable Mie cases. However, it is noted that the
 10 reduced normalized Mie phase matrix can be steadily and accurately computed over a wide frequency
 11 range (in terms of mean size parameter $\langle x \rangle$) since there exist numerically stable algorithms [17], [18],
 12 [23], [24] for frequencies up to at least ~ 1000 GHz and for practical hydrometer size distributions. In
 13 contrast there is no conclusive study on the stability of the DMRT-QCA algorithm except for a brief
 14 discussion of the maximum number N_{max} of L-L equations required for convergence in [11]. From this
 15 work N_{max} is suggested to be determined by the relation $N_{max} = \text{round}(k \langle D \rangle) + 1$. This requirement for
 16 N_{max} was studied by computing the DMRT-QCA phase matrices at frequencies up to 1000 GHz. First, it
 17 should be pointed out that in the three cases of Fig. 4 the errors caused by the choice of N_{max} are small
 18 (the value of N_{max} is 4 at 100 GHz). As the frequency is extended to 300 GHz a value $N_{max} = 10$ is
 19 needed, thus increasing the computational burden. The L-L system of equations becomes ill-conditioned
 20 at higher frequencies and a stable numerical solution is currently unavailable. Nonetheless, for microwave
 21 remote sensing of snow and ice, DMRT-QCA is still readily computable for the most practical snow and
 22 ice sensing frequencies (i.e., below ~ 100 GHz).
 23
 24
 25
 26
 27
 28
 29
 30
 31
 32
 33
 34
 35
 36
 37
 38
 39
 40
 41
 42
 43
 44

45 III. UMRT FRAMEWORK

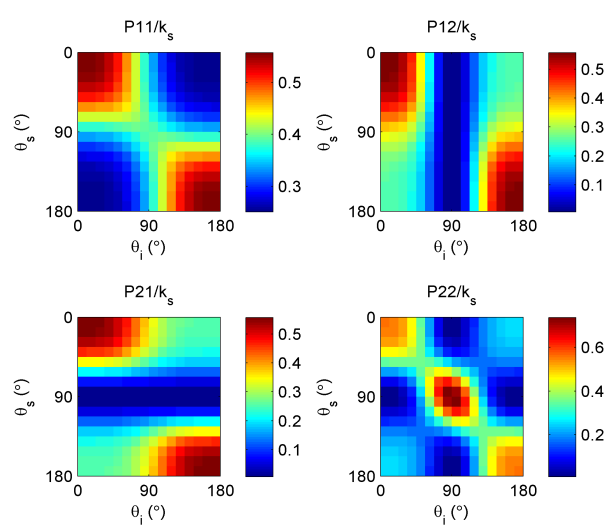
46 A. DRTE Symmetrization

47 UMRT assumes a planar stratified medium structure and provides a solution for the brightness
 48 temperature $T_B(\theta, z)$ in upwelling (+) and downwelling (−) directions, accounting for polarization
 49 coupling caused by the reduced phase matrix. The differential radiative transfer equation (DRTE) is
 50 discretized over a set of quadrature angles θ_i , which are determined by the Gauss-Legendre nodes and
 51 Christoffel weights:
 52
 53
 54
 55
 56
 57
 58
 59
 60

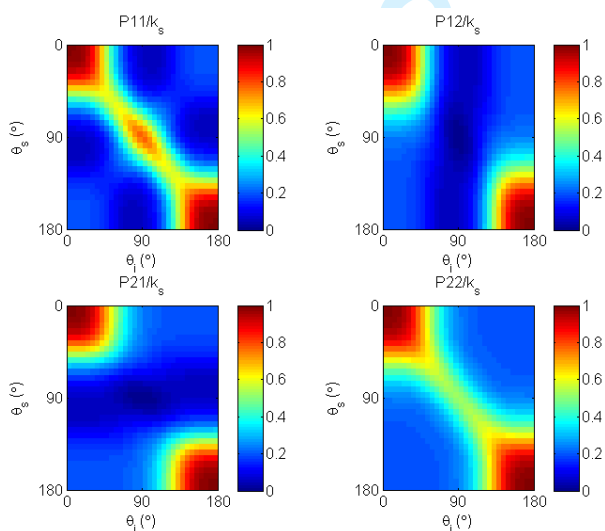
1
2
3
4
5
6
7
8
9
10
11
12
13
14
15
16
17
18
19
20
21
22
23
24
25
26
27
28
29
30
31
32
33
34
35
36
37
38
39
40
41
42
43
44
45
46
47
48
49
50
51
52
53
54
55
56
57
58
59
60



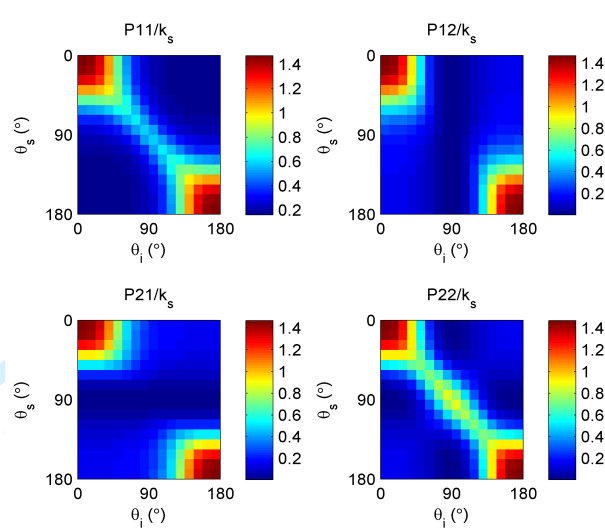
(a) 10 GHz



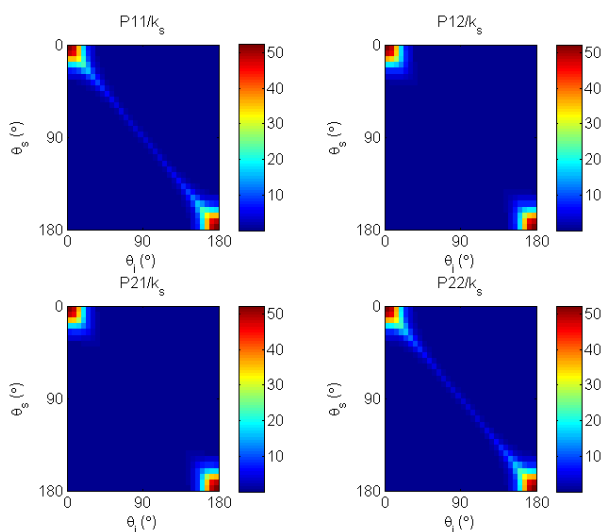
(a) 10 GHz



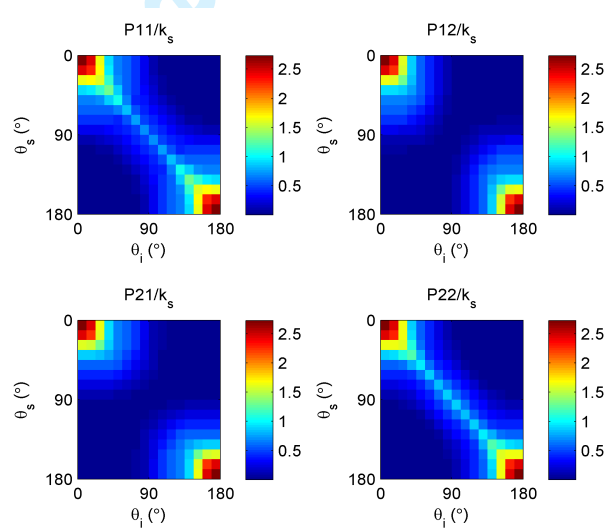
(b) 100 GHz



(b) 30 GHz



(c) 1000 GHz



(c) 100 GHz

Figure 3. Reduced normalized Mie phase matrices using an MP rain distribution of 10 mm/hr and 32 quadrature angles.

Figure 4. Reduced normalized DMRT-QCA phase matrices for a sticky Percus-Yevick pair distribution using 16 quadrature angles.

$$\begin{aligned} \mu_i \frac{dT_{Bvi}^+}{dz} = & -k_e T_{Bvi}^+ + \left[\sum_{j=1}^M \gamma_j P_{vvi}^{++} T_{Bvj}^+ + \sum_{j=1}^M \gamma_j P_{vvi}^{+-} T_{Bvj}^- \right. \\ & \left. + \sum_{j=1}^M \gamma_j P_{vhi}^{++} T_{Bhj}^+ + \sum_{j=1}^M \gamma_j P_{vhi}^{+-} T_{Bhj}^- \right] + k_a T(z) \end{aligned} \quad (31)$$

$$\begin{aligned} -\mu_i \frac{dT_{Bvi}^-}{dz} = & -k_e T_{Bvi}^- + \left[\sum_{j=1}^M \gamma_j P_{vvi}^{-+} T_{Bvj}^+ + \sum_{j=1}^M \gamma_j P_{vvi}^{--} T_{Bvj}^- \right. \\ & \left. + \sum_{j=1}^M \gamma_j P_{vhi}^{-+} T_{Bhj}^+ + \sum_{j=1}^M \gamma_j P_{vhi}^{--} T_{Bhj}^- \right] + k_a T(z) \end{aligned} \quad (32)$$

$$\begin{aligned} \mu_i \frac{dT_{Bhi}^+}{dz} = & -k_e T_{Bhi}^+ + \left[\sum_{j=1}^M \gamma_j P_{hvi}^{++} T_{Bvj}^+ + \sum_{j=1}^M \gamma_j P_{hvi}^{+-} T_{Bvj}^- \right. \\ & \left. + \sum_{j=1}^M \gamma_j P_{hhi}^{++} T_{Bhj}^+ + \sum_{j=1}^M \gamma_j P_{hhi}^{+-} T_{Bhj}^- \right] + k_a T(z) \end{aligned} \quad (33)$$

$$\begin{aligned} -\mu_i \frac{dT_{Bhi}^-}{dz} = & -k_e T_{Bhi}^- + \left[\sum_{j=1}^M \gamma_j P_{hvi}^{-+} T_{Bvj}^+ + \sum_{j=1}^M \gamma_j P_{hvi}^{--} T_{Bvj}^- \right. \\ & \left. + \sum_{j=1}^M \gamma_j P_{hhi}^{-+} T_{Bhj}^+ + \sum_{j=1}^M \gamma_j P_{hhi}^{--} T_{Bhj}^- \right] + k_a T(z) \end{aligned} \quad (34)$$

where $\mu_i = \cos\theta_i$, γ_j are the Christoffel weights, and M is the number of quadrature angles between zenith and the horizon. Here, we choose $M = 16$ in this study, which is suitable for most passive remote sensing purposes. All μ_i in the above equations are positive as a result of separating the brightness temperature in the up- and down-welling directions. Following [1], and with reference to (21), the discretized reduced phase matrix elements are defined as

$$\begin{aligned} P_{\alpha\beta ij}^{++} &= P_{\alpha\beta}(\mu_i, \mu_j) & P_{\alpha\beta ij}^{+-} &= P_{\alpha\beta}(\mu_i, -\mu_j) \\ P_{\alpha\beta ij}^{-+} &= P_{\alpha\beta}(-\mu_i, \mu_j) & P_{\alpha\beta ij}^{--} &= P_{\alpha\beta}(-\mu_i, -\mu_j) \end{aligned} \quad (35)$$

where α, β are either v (vertical) or h (horizontal) polarization. As shown in §2 the reduced Mie and DMRT-QCA phase matrices are symmetric with respect to simultaneous permutation of angular indexes and independent permutations of both up- and down-welling indexes:

$$\begin{aligned} P_{\alpha\beta ij}^{++} &= P_{\alpha\beta ji}^{++} & P_{\alpha\beta ij}^{--} &= P_{\alpha\beta ji}^{--} & P_{\alpha\beta ij}^{-+} &= P_{\alpha\beta ji}^{-+} \\ P_{\alpha\beta ij}^{+-} &= P_{\alpha\beta ji}^{--} & P_{\alpha\beta ij}^{-+} &= P_{\alpha\beta ji}^{+-} \end{aligned} \quad (36)$$

Following [1], new variables for the up- and down-welling streams are introduced to make the DRTE explicitly symmetric:

$$\begin{aligned} u_{vi} &= \sqrt{\mu_i \gamma_i} T_{Bvi}^+ & u_{hi} &= \sqrt{\mu_i \gamma_i} T_{Bhi}^+ \\ v_{vi} &= \sqrt{\mu_i \gamma_i} T_{Bvi}^- & v_{hi} &= \sqrt{\mu_i \gamma_i} T_{Bhi}^- \end{aligned} \quad (37)$$

By rearranging (31-34) with the above new variables the following matrix form of discretized DRTE equations is obtained:

$$\begin{aligned} \underbrace{\frac{d}{dz} \begin{bmatrix} \bar{u}_v \\ \bar{u}_h \\ \bar{v}_v \\ \bar{v}_h \end{bmatrix}}_{4M \times 1} &= \underbrace{\begin{bmatrix} -\bar{A}_0 & -\bar{C}_0 & -\bar{B}_0 & -\bar{D}_0 \\ -\bar{E}_0 & -\bar{G}_0 & -\bar{F}_0 & -\bar{H}_0 \\ \bar{B}_0 & \bar{D}_0 & \bar{A}_0 & \bar{C}_0 \\ \bar{F}_0 & \bar{H}_0 & \bar{E}_0 & \bar{G}_0 \end{bmatrix}}_{4M \times 4M} \underbrace{\begin{bmatrix} \bar{u}_v \\ \bar{u}_h \\ \bar{v}_v \\ \bar{v}_h \end{bmatrix}}_{4M \times 1} + \underbrace{\begin{bmatrix} \bar{f} \\ \bar{f} \\ -\bar{f} \\ -\bar{f} \end{bmatrix}}_{4M \times 1} \\ &= \underbrace{\begin{bmatrix} -\bar{U} & -\bar{D} \\ \bar{D} & \bar{U} \end{bmatrix}}_{\text{DOTLRT}} \underbrace{\begin{bmatrix} \bar{u} \\ \bar{v} \end{bmatrix}}_{4M \times 1} + \underbrace{\begin{bmatrix} \bar{F} \\ -\bar{F} \end{bmatrix}}_{4M \times 1} \end{aligned} \quad (38)$$

where $\bar{u} \triangleq \begin{bmatrix} \bar{u}_v \\ \bar{u}_h \end{bmatrix}$, $\bar{v} \triangleq \begin{bmatrix} \bar{v}_v \\ \bar{v}_h \end{bmatrix}$, $\bar{F} \triangleq \begin{bmatrix} \bar{f} \\ \bar{f} \end{bmatrix}$, $\bar{U} \triangleq \begin{bmatrix} \bar{A}_0 & \bar{C}_0 \\ \bar{E}_0 & \bar{G}_0 \end{bmatrix}$, and $\bar{D} \triangleq \begin{bmatrix} \bar{B}_0 & \bar{D}_0 \\ \bar{F}_0 & \bar{H}_0 \end{bmatrix}$. The sub-matrices for vertical and horizontal polarization are defined as

$$\begin{aligned} A_{0ij} &= \frac{k_e}{\mu_i} \delta_{ij} - \sqrt{\frac{\gamma_i \gamma_j}{\mu_i \mu_j}} P_{vvi}^{++} & B_{0ij} &= -\sqrt{\frac{\gamma_i \gamma_j}{\mu_i \mu_j}} P_{vvi}^{+-} \\ C_{0ij} &= -\sqrt{\frac{\gamma_i \gamma_j}{\mu_i \mu_j}} P_{vhi}^{++} & D_{0ij} &= -\sqrt{\frac{\gamma_i \gamma_j}{\mu_i \mu_j}} P_{vhi}^{+-} \\ E_{0ij} &= -\sqrt{\frac{\gamma_i \gamma_j}{\mu_i \mu_j}} P_{hvi}^{++} & F_{0ij} &= -\sqrt{\frac{\gamma_i \gamma_j}{\mu_i \mu_j}} P_{hvi}^{+-} \\ G_{0ij} &= \frac{k_e}{\mu_i} \delta_{ij} - \sqrt{\frac{\gamma_i \gamma_j}{\mu_i \mu_j}} P_{hhi}^{++} & H_{0ij} &= -\sqrt{\frac{\gamma_i \gamma_j}{\mu_i \mu_j}} P_{hhi}^{+-} \end{aligned} \quad (39)$$

The vector \bar{f} represents thermal emission from the medium and is defined by $f_i = \sqrt{\frac{\gamma_i}{\mu_i}} k_a T_m$, where $T_m \triangleq (T_o - \gamma z)$ and γ is the temperature lapse rate.

Finally, the boundary conditions are

$$\begin{aligned} \mu_i T_{\beta i}^+ &= \sum_{j=1}^M \gamma_j s_{\beta ij} T_{B\beta i}^- + \left(\mu_i - \sum_{j=1}^M \gamma_j s_{\beta ji} \right) T_s, \quad z = 0 \\ T_{\beta i}^- &= T_{cb}, \quad z = H \end{aligned} \quad (40)$$

where T_{cb} is the cosmic background temperature at the topmost atmospheric level $z = H$, T_s is the surface background temperature, and in the case of a specular surface the surface bistatic function s_{ij} is obtained using the Fresnel reflection coefficient R_i as

$$s_{\beta ij} = \mu_i |R_{\beta i}|^2 \delta_{ij}, \quad \gamma_j = 1 \quad (41)$$

For coupled vertical-horizontal radiation streams all sub-matrices in $\overline{\overline{U}}$ and $\overline{\overline{D}}$ are defined from specific reduced phase matrices, which have been shown to be symmetric with respect to incident and scattering angles. Thus both matrices $\overline{\overline{U}}$ and $\overline{\overline{D}}$ are symmetric along with the following two new matrices: $\overline{\overline{A}} \triangleq \overline{\overline{U}} + \overline{\overline{D}}$ and $\overline{\overline{B}} \triangleq \overline{\overline{U}} - \overline{\overline{D}}$.

B. Solution for A Single Layer

UMRT assumes a planar-stratified stack of reciprocal homogenous layers in which the medium properties are assumed constant and the source vector $\overline{\overline{F}}$ is at most linear in height (Fig. 5(a)). In addition to the extension to multiple coupled Stokes parameters, the assumption of the kinetic temperature of a layer being linear is another fundamental difference between UMRT and DOTLRT.

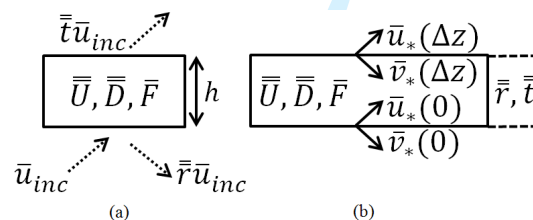


Figure 5. (a) Matrix representation of the reflection and transmission matrix operators, and (b) self-radiation stream vectors for a single layer.

Owing to thermal emission, the layer will generate self-radiation streams in the up- (u) and down- (v) welling directions at its top and bottom surfaces, respectively. Such streams denoted by the subscript $*$ (Fig. 5(b)). To solve for them it is required to compute the reflection and transmission matrices ($\overline{\overline{r}}$ and $\overline{\overline{t}}$) which describe the volumetric scattering inside the layer. The layer is assumed to be embedded within a homogeneous dielectric environment of permittivity equal to the effective permittivity of the layer. As such, there is no surface Fresnel reflection at the interfaces to this neutral dielectric background environment. Assuming an external radiation field \overline{u}_{inc} incident from the bottom of the layer (Fig. 5(a)), we define the reflection and transmission matrices implicitly by

$$\begin{aligned}\bar{u} &= \bar{t} \bar{u}_{inc} \quad \text{at } z = h \\ \bar{v} &= \bar{r} \bar{u}_{inc} \quad \text{at } z = 0\end{aligned}\tag{42}$$

These matrices can be found using the homogeneous solution to the DRTE, written as:

$$\begin{bmatrix} \bar{u}(z) \\ \bar{v}(z) \end{bmatrix} = \frac{1}{2} \begin{bmatrix} 1 & 1 \\ -1 & 1 \end{bmatrix} \begin{bmatrix} \bar{c} & -\bar{s}\bar{A} \\ -\bar{B}\bar{s} & \bar{c}^T \end{bmatrix} \begin{bmatrix} 1 & -1 \\ 1 & 1 \end{bmatrix} \begin{bmatrix} \bar{u}(0) \\ \bar{v}(0) \end{bmatrix}\tag{43}$$

Applying (42) we have

$$\begin{bmatrix} \bar{t} \bar{u}_{inc} \\ 0 \end{bmatrix} = \frac{1}{2} \begin{bmatrix} \bar{c} - \bar{B}\bar{s} - \bar{s}\bar{A} + \bar{c}^T & -\bar{c} + \bar{B}\bar{s} - \bar{s}\bar{A} + \bar{c}^T \\ -\bar{c} - \bar{B}\bar{s} + \bar{s}\bar{A} + \bar{c}^T & \bar{c} + \bar{B}\bar{s} + \bar{s}\bar{A} + \bar{c}^T \end{bmatrix} \begin{bmatrix} \bar{u}_{inc} \\ \bar{r} \bar{u}_{inc} \end{bmatrix}\tag{44}$$

where the matrices \bar{c} and \bar{s} are defined as

$$\begin{aligned}\bar{c} &\triangleq \cosh(\sqrt{\bar{A}\bar{B}}h) \\ \bar{s} &\triangleq \sinh(\sqrt{\bar{A}\bar{B}}h) \cdot (\bar{A}\bar{B})^{-\frac{1}{2}}\end{aligned}\tag{45}$$

and are evaluated at $z = h$. From (44) we obtain

$$\begin{aligned}\bar{t} &= 2 \left(\bar{c} + \bar{B}\bar{s} + \bar{s}\bar{A} + \bar{c}^T \right)^{-1} \triangleq 2\bar{Q}^{-1} \\ \bar{r} &= \bar{Q}^{-1} \left(\bar{c} + \bar{B}\bar{s} - \bar{s}\bar{A} - \bar{c}^T \right)\end{aligned}\tag{46}$$

It is noted that the above matrices exhibit the symmetry necessary as a result of reciprocity.

$$\bar{r} = \bar{r}^T \quad \text{and} \quad \bar{t} = \bar{t}^T\tag{47}$$

Although the above procedure is analytically correct, the direct inversion of the matrix \bar{Q} will usually fail numerically when the medium layer is either highly opaque or thick or both. The problem is that the matrix functions \bar{c} and \bar{s} are functions of $\cosh(x)$ and $\sinh(x)$, respectively. Such hyperbolic functions contain fast growing exponentials which quickly lead to ill-conditioning of \bar{Q} . To circumvent this problem DOTLRT uses equations (2-6) along with analytical diagonalization and factorization of the constituent symmetric and positive definite matrices that comprise \bar{Q} to represent it as

$$\bar{Q} = \bar{M}_1 \bar{a} \bar{\zeta} \bar{b}_t \bar{M}_1^T\tag{48}$$

Thus, the matrices $\bar{\bar{r}}$ and $\bar{\bar{t}}$ are readily computed as follows:

$$\begin{aligned}\bar{\bar{t}} &= 2\bar{\bar{M}}_1\bar{\bar{b}}_t^{-1}\bar{\bar{\zeta}}^{-1}\bar{\bar{a}}^{-1}\bar{\bar{M}}_1^T \\ \bar{\bar{r}} &= \bar{\bar{t}} - \bar{\bar{M}}_1\bar{\bar{b}}_t^{-1}\bar{\bar{b}}_r\bar{\bar{M}}_1^T\end{aligned}\quad (49)$$

In (48-49), the matrix $\bar{\bar{M}}_1$ is the orthogonal matrix consisting of the column eigenvectors of the matrix $\bar{\bar{A}}$. The matrices $\bar{\bar{b}}_t$, $\bar{\bar{b}}_r$ and $\bar{\bar{a}}$ are transitional matrix functions involving $\tanh(x)$ and $\coth(x)$, where x is a function of the layer thickness. Since both $\tanh(x)$ and $\coth(x)$ are bounded to 1 as $x \rightarrow \infty$ the matrices $\bar{\bar{b}}_t$, $\bar{\bar{b}}_r$ and $\bar{\bar{a}}$ tend to finite limits. The matrix $\bar{\bar{\zeta}}$ is a diagonal matrix function containing terms in $\sinh(x)$. Since $\bar{\bar{\zeta}}$ is diagonal, it is always precisely invertible. Details of the matrices $\bar{\bar{b}}_t$, $\bar{\bar{b}}_r$, $\bar{\bar{a}}$, and $\bar{\bar{\zeta}}$ are well defined in ([1], eqs. 51-56).

For a layer with constant temperature profile (i.e., $\gamma = 0$) DOTLRT computes the self-radiation stream vectors as follows

$$\begin{aligned}\bar{u}_*(0) &= \bar{v}_*(0) = (\bar{\bar{I}} - \bar{\bar{r}} - \bar{\bar{t}}) \bar{u}_{inh} \\ \bar{u}_*(h) &= \bar{u}_*(h) \\ \bar{v}_*(h) &= \bar{v}_*(h)\end{aligned}\quad (50)$$

where $\bar{\bar{I}} - \bar{\bar{r}} - \bar{\bar{t}}$ can be interpreted as an effective emissivity matrix for the layer. The inhomogeneous solution of the DRTE (38) is

$$\begin{bmatrix} \bar{u}_{inh} \\ \bar{v}_{inh} \end{bmatrix} = \begin{bmatrix} (\bar{\bar{U}} + \bar{\bar{D}})^{-1} \bar{\bar{F}} \\ (\bar{\bar{U}} + \bar{\bar{D}})^{-1} \bar{\bar{F}} \end{bmatrix} = \begin{bmatrix} \bar{\bar{A}}^{-1} \bar{\bar{F}} \\ \bar{\bar{A}}^{-1} \bar{\bar{F}} \end{bmatrix}\quad (51)$$

Extending the above to the case of a linear temperature profile the inhomogeneous DRTE is solved by assuming $\bar{u}_{inh}(z) = \bar{u}_o - \bar{u}_1 z$, $\bar{v}_{inh}(z) = \bar{v}_o - \bar{v}_1 z$, $F_i(z) \triangleq \sqrt{\frac{\gamma_i}{\mu_i}} k_a (T_o - \gamma z) \triangleq F_{oi} - \gamma_{Ti} z$, where $F_{oi} = \sqrt{\frac{\gamma_i}{\mu_i}} k_a T_o$ and $\gamma_{Ti} = \sqrt{\frac{\gamma_i}{\mu_i}} k_a \gamma$. Substituting these quantities into the DRTE yields

$$\begin{aligned}\begin{bmatrix} -\bar{u}_1 \\ -\bar{v}_1 \end{bmatrix} &= \begin{bmatrix} -\bar{\bar{U}} & -\bar{\bar{D}} \\ \bar{\bar{D}} & \bar{\bar{U}} \end{bmatrix} \begin{bmatrix} \bar{u}_o - \bar{u}_1 z \\ \bar{v}_o - \bar{v}_1 z \end{bmatrix} \\ &+ \begin{bmatrix} \bar{\bar{F}}_o - \bar{\gamma}_T z \\ -\bar{\bar{F}}_o + \bar{\gamma}_T z \end{bmatrix}\end{aligned}\quad (52)$$

Balancing (52) and applying block matrix inversion [25] along with some simple linear algebra, we

obtain

$$\begin{bmatrix} \bar{u}_{inh}(z) \\ \bar{v}_{inh}(z) \end{bmatrix} = \begin{bmatrix} \bar{A}^{-1} \bar{F}(z) + \bar{B}^{-1} \bar{A}^{-1} \bar{\gamma}_T \\ \bar{A}^{-1} \bar{F}(z) - \bar{B}^{-1} \bar{A}^{-1} \bar{\gamma}_T \end{bmatrix} \quad (53)$$

Note that if $\gamma = 0$ (77) is reduced to (51). The connection between the inhomogeneous solutions, \bar{u}_{inh} and \bar{v}_{inh} , and the upwelling self-radiation stream vector \bar{u}_* is illustrated in Fig. 6 where two artificial external radiation stream vectors $\bar{v}_{inh}(h)$ incident on the top of the layer from above and $\bar{u}_{inh}(0)$ incident on the bottom of the layer from below are assumed. The two incident stream vectors will correspondingly produce two additional stream vectors at the top of the layer equal to $\bar{r} \bar{v}_{inh}(h)$ and $\bar{t} \bar{u}_{inh}(0)$, illustrated in Fig. 6(b).

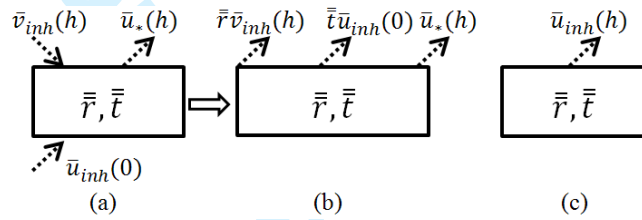


Figure 6. Calculation of the upwelling self-radiation for a single layer with linear temperature profile.

Adding all of the stream components in Fig. 6(b) results in the following expression for the upwelling inhomogeneous solution at the top of the layer in terms of \bar{r} and \bar{t} :

$$\bar{u}_{inh}(h) = \bar{u}_*(h) + \bar{r} \bar{v}_{inh}(h) + \bar{t} \bar{u}_{inh}(0) \quad (54)$$

Rearranging (54) the upwelling self-radiation stream vector can be expressed as

$$\bar{u}_*(h) = \bar{u}_{inh}(h) - \bar{r} \bar{v}_{inh}(h) - \bar{t} \bar{u}_{inh}(0) \quad (55)$$

Similarly, the downwelling self-radiated stream vector is

$$\bar{v}_*(0) = \bar{v}_{inh}(0) - \bar{r} \bar{u}_{inh}(0) - \bar{t} \bar{v}_{inh}(h) \quad (56)$$

The above solutions (55-56) extend DOTLRT to make UMRT a more widely applicable polarimetric (three Stokes parameter) and level-centric (rather than layer-centric) discrete-ordinate radiative transfer solution .

C. Solution for a Multilayer Stack

Using the single-layer solution a procedure for solving for the total radiated and reflected stream vectors for a multilayer stack with non-refracting boundaries can be developed. Once the matrices $\bar{\bar{r}}$ and $\bar{\bar{t}}$ for all individual layers and the vectors \bar{u}_* and \bar{v}_* at all levels are obtained, the overall radiative characteristics of the stack, $\bar{\bar{R}}^{(n+1)}$ and $\bar{\bar{U}}_*^{(n+1)}$ can be calculated by upward recursion. Since the vectors \bar{u}_* and \bar{v}_* are fundamentally different for a layer with linear temperature profile versus a constant-temperature layer the upward recursive formulae of DOTLRT are modified as follows

$$\bar{\bar{U}}_*^{(n+1)} = \bar{u}_*^{(n+1)} + \bar{\bar{t}}^{(n+1)} \left(\bar{\bar{I}} - \bar{\bar{R}}^{(n)} \bar{\bar{r}}^{(n+1)} \right)^{-1} \cdot \left(\bar{\bar{U}}_*^{(n)} + \bar{\bar{R}}^{(n)} \bar{v}_*^{(n+1)} \right) \quad (57)$$

$$\bar{\bar{R}}^{(n+1)} = \bar{\bar{r}}^{(n+1)} + \bar{\bar{t}}^{(n+1)} \left(\bar{\bar{I}} - \bar{\bar{R}}^{(n)} \bar{\bar{r}}^{(n+1)} \right)^{-1} \bar{\bar{R}}^{(n)} \bar{\bar{t}}^{(n+1)} \quad (58)$$

where the uppercase characters denote characteristics of a stack in order to distinguish them with their counterparts for a single layer.

The boundary conditions for the stack are:

$$\bar{\bar{U}}_*^{(0)} = \bar{F}^{(0)} \quad \text{and} \quad \bar{\bar{R}}^{(0)} = \bar{\bar{S}} \quad (59)$$

where $\bar{F}^{(0)}$ denotes the upwelling stream vector from the bounding lower half space and $\bar{\bar{S}}$ is defined by the surface bistatic scattering function of the lower half space

$$S_{\beta ij} = \sqrt{\frac{\gamma_i \gamma_j}{\mu_i \mu_j}} s_{\beta ij} \quad (60)$$

It should be noted point that all of the above stream vectors ($\bar{\bar{U}}_*$, \bar{u}_* , \bar{v}_*), reflection matrices ($\bar{\bar{R}}$, $\bar{\bar{r}}$) and transmission matrices ($\bar{\bar{t}}$) are calculated assuming that each single layer or stack has non-refractive boundaries. For this simple case the UMRT Jacobian procedure is analogous to that of DOTLRT except for two aspects: 1) the phase matrix is extended in polarization, including the exact Mie and DMRT-QCA phase matrices so that the associated Jacobian calculations must correspondingly be extended, and 2) the physical temperature profile of a layer is extended from being constant to linear, thus the UMRT Jacobian includes the temperature lapse rate and the difference in the up- and down-welling self-radiation

streams needs to be considered. Further, if the stack contains refractive boundaries then the above recursive equations need to be correspondingly modified, along with the UMRT Jacobian procedure. The details of such a refractive extension are provided in [26].

IV. NUMERICAL EXAMPLES

The calculations of self-radiation streams and reflection and transmission matrices for a single layer are validated by imposing energy conservation. The validation scheme is depicted in Fig. 7. In Fig. 7, we assume a single layer with constant physical temperature T_o is embedded in a homogeneous background environment whose physical temperature is also T_o . This scenario results in down- and up-welling radiation streams \bar{v}_{inc} and \bar{u}_{inc} impinging on the layer. From thermodynamic equilibrium the brightness temperature of the sum of $\bar{u}_* + \bar{r}\bar{v}_{inc} + \bar{t}\bar{u}_{inc}$ must equal to T_o at all observation angles. As recorded in Tab. II, the UMRT model was tested for this condition using four reduced phase matrices (HG, Rayleigh, Mie, and DMRT-QCA), and two nominal materials (water and dry snow). For the first three reduced phase matrices, the validation was performed up to 1000 GHz in frequency, employing a single rain layer model with 1 km thickness and under the Marshall-Palmer (MP) size distribution with precipitation = 10 mm/hr. For the reduced DMRT-QCA phase matrix, validation was performed at frequencies up to 100 GHz using a 1 m thick dry snow layer with the following parameters: $f_v = 0.25$, $\tau = 0.1$, and $\langle D \rangle = 1.4$ mm. The error between the brightness temperature computed by UMRT and T_o at the i^{th} angle is defined as

$$\varepsilon_{\max}(\theta_i) = \left| \frac{\left(\bar{u}_* + \bar{r}\bar{v}_{inc} + \bar{t}\bar{u}_{inc} \right)_i}{\sqrt{\mu_i \gamma_i}} - T_o \right| \quad (61)$$

As shown in Tab. II, the maximum absolute error of the various phase matrix cases is of order 10^{-10} to 10^{-13} K over sixteen discrete observation angles. This error can be ascribed to roundoff error associated with IEEE standard arithmetic.

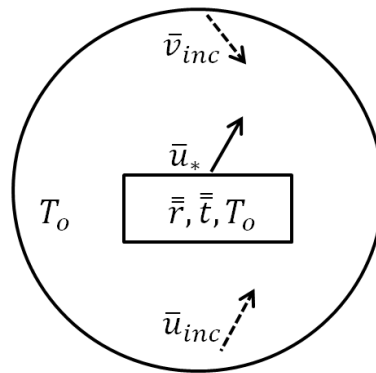


Figure 7. The UMRT validation scheme of energy conservation

Table II
VALIDATION OF FOUR PHASE MATRICES USING ENERGY CONSERVATION.

Test Conditions	Max. Error (K)
HG, Water, Frequencies up to 10^3 GHz	$\sim 10^{-13}$
Rayleigh, Water, Frequencies up to 10^3 GHz	$\sim 10^{-13}$
Mie, Water, Frequencies up to 10^3 GHz	$\sim 10^{-13}$
DMRT, Dry Snow, Frequencies up to 10^2 GHz	$\sim 10^{-10}$

Next, a single rain layer is used as an example to compare the brightness temperatures computed by UMRT assuming each of three reduced phase matrices: Rayleigh, HG, and Mie. Both constant and linear temperature profiles were tested for this layer. The MP size distribution is assumed and the water permittivity is determined by Meissner and Wentz's double Debye expression [22]. The test details are provided in Tab. III.

Table III
SINGLE RAIN LAYER UNDER THE MARSHALL-PALMER (MP) SIZE DISTRIBUTION.

Layer	Temperature (K)	Rain Rate	$\langle D \rangle$ (mm)	Frequency (GHz)
Water, 1 km	300	10 mm/hr	0.40	10.7, 18.6, 37.0
Water, 1 km	300 to 273	10 mm/hr	0.40	10.7, 18.6, 37.0

For the layer with a constant 300 K temperature the emitted brightness temperatures were computed for the three phase matrices at three distinct frequencies (10.7, 18.6 and 37.0 GHz), and categorized by direction (up- and down-welling) and polarization (horizontal and vertical) (see Fig. 8). From Fig. 8, we see that at the two low frequencies (10.7 and 18.6 GHz) the brightness temperatures for the three phase matrices are nearly identical while at the high frequency (37.0 GHz), the Rayleigh and HG cases are slightly colder (~ 2 K) than that of the Mie case. We also note that all three phase matrices yield identical upwelling and downwelling radiation streams, which is expected for a uniform temperature

profile. We also see that in both Rayleigh and HG, the horizontal brightness temperatures equal their vertical counterparts, as expected from the decoupled polarization characteristic of both Rayleigh and HG phase matrices. However, the Mie phase matrix shows clear differences between the horizontal and vertical brightness temperatures of ~ 6 K, particularly at the frequencies approaching the transition from the Rayleigh to the Mie region.

For the layer with a linear temperature profile the brightness temperatures are plotted in Fig. 9. Comparing Figs. 8 and 9 there is similar general behavior in both cases. However, the downwelling radiation streams are considerably greater than their corresponding upwelling counterparts, which is what is expected given the linear temperature profile.

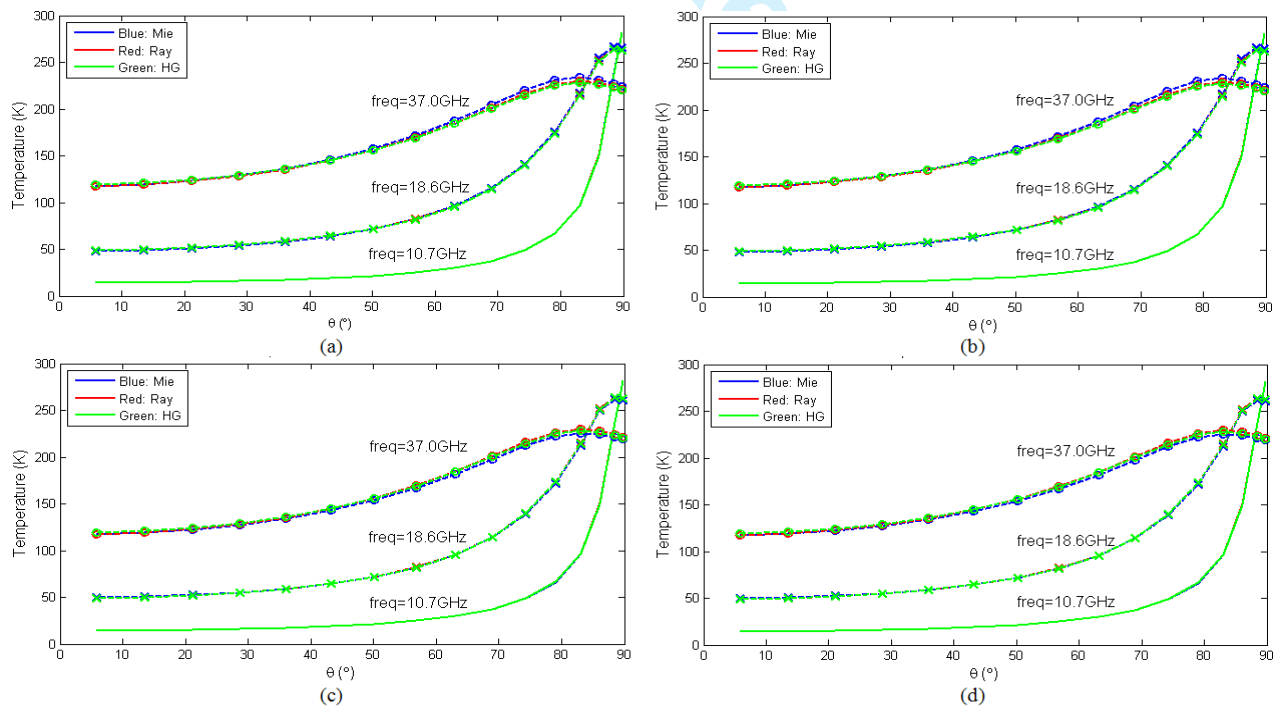


Figure 8. Brightness temperatures for a rain layer with a constant temperature profile: (a) horizontal-upwelling, (b) horizontal-downwelling, (c) vertical-upwelling, and (d) vertical-downwelling. Blue, red and green plots are made using the Mie, Rayleigh, and HG phase matrices, respectively.

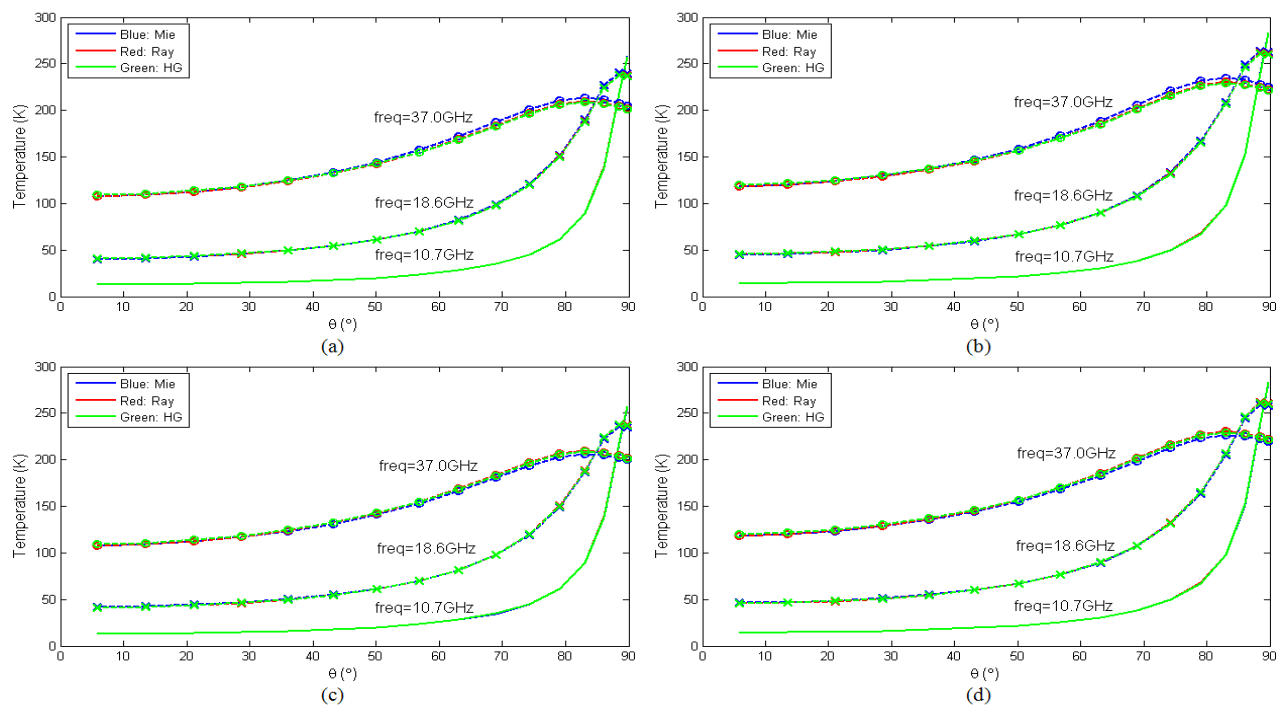


Figure 9. Brightness temperatures for a rain layer with a linear temperature profile: (a) horizontal-upwelling, (b) horizontal-downwelling, (c) vertical-upwelling, and (d) vertical-downwelling. Blue, red and green plots are made using the Mie, Rayleigh, and HG phase matrices, respectively.

Similarly, the polarized brightness temperatures emitted in the up- and down-welling directions from a single dry snow layer with 0.1 m thickness at four frequencies (10.7, 18.6, 37.0 and 89.0 GHz) were studied (Figs. 10 and 11). The test details are provided in Tab. IV. From Figs. 10 and 11, the differences in brightness temperatures due to different temperature profiles are seen. It is noted that as frequency increases, the brightness temperatures at normal incidence decrease, which is what expected since the snow layer appears less emissive at higher frequencies.

Table IV
SINGLE DRY SNOW LAYER USING THE REDUCED DMRT-QCA PHASE MATRIX.

Layer	Temperature (K)	f_v	τ	$\langle D \rangle$ (mm)	Frequency (GHz)
Snow, 0.1 m	273	0.25	0.1	1.4	10.7, 18.6, 37.0, 89.0
Snow, 0.1 m	273 to 253	0.25	0.1	1.4	10.7, 18.6, 37.0, 89.0

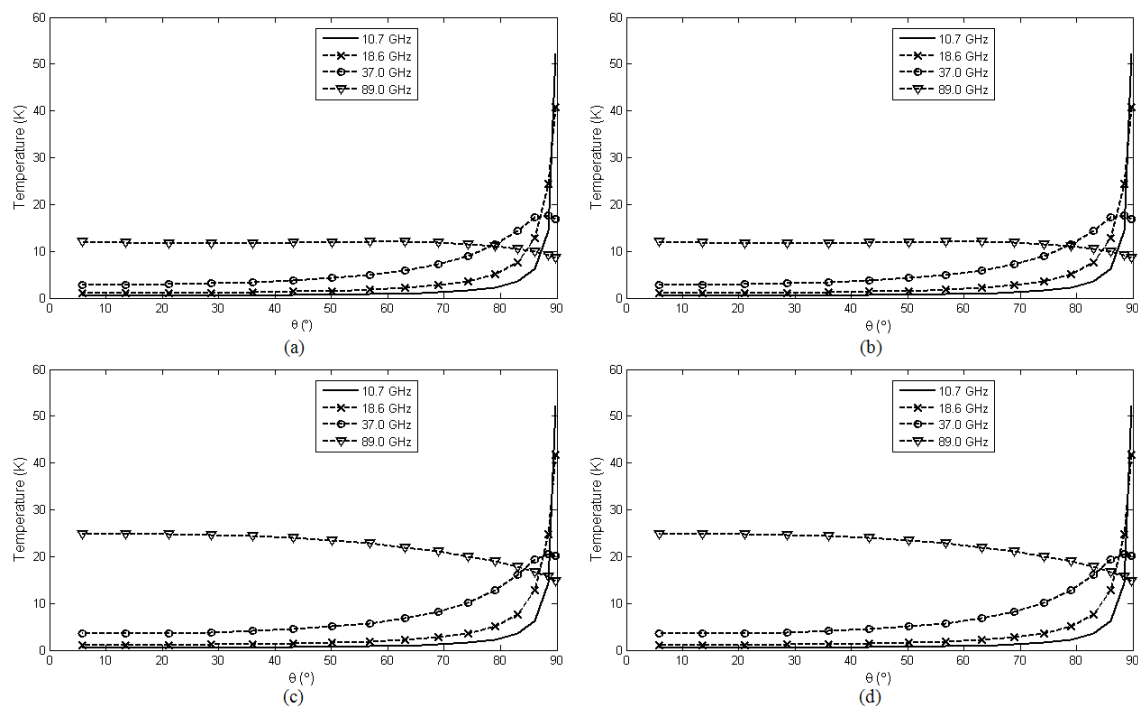


Figure 10. Brightness temperatures for a dry snow layer with a constant temperature profile: (a) horizontal-upwelling, (b) horizontal-downwelling, (c) vertical-upwelling, and (d) vertical-downwelling.

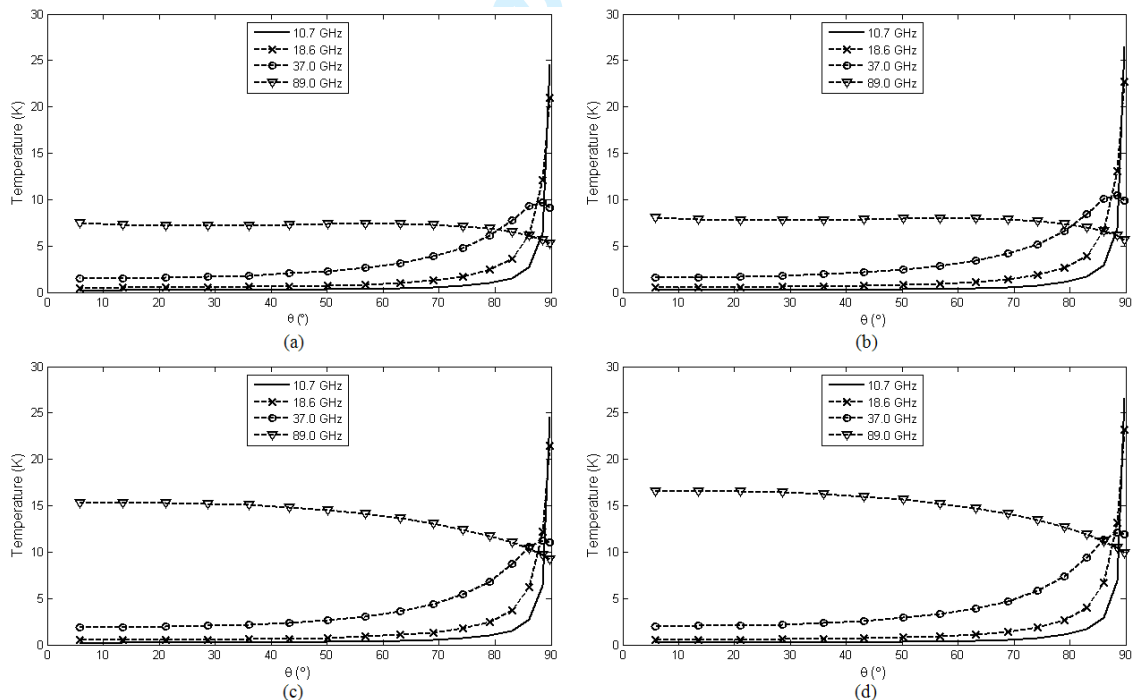


Figure 11. Brightness temperatures for a dry snow layer with a linear temperature profile: (a) horizontal-upwelling, (b) horizontal-downwelling, (c) vertical-upwelling, and (d) vertical-downwelling.

V. CONCLUSIONS

Presented is a new unified microwave radiative transfer (UMRT) model for accurate, fast and stable calculation of thermal radiation from any geophysical medium comprised of planar multilayer spherical

scatters of arbitrary electrical size. UMRT combines several unique new features from discrete ordinate radiative transfer theory and dense media radiative transfer theory under the DOTLRT framework for calculating the thermal radiation from either sparse or dense media. Other important features of UMRT include: 1) the inherent stability and high computational efficiency of recursive matrix calculations performed for both the brightness temperatures and associated Jacobians, 2) application of the reduced Mie and DMRT-QCA phase matrices, 3) incorporation of linear radiation and temperature profiles within each layer, and 4) use of the critical angle and Fresnel effects at layer interfaces (discussed elsewhere in [26]). As a result of these extensions UMRT is applicable to real-time all-weather microwave radiance assimilation in both clear and cloud atmospheres and over both simple and dense volume-scattering media for both atmospheric and surface nowcasting and forecasting. In developing the above model, the symmetry properties of both the Mie and DMRT-QCA phase matrices relevant for use in DOTLRT are proven and the associated scattering and absorption coefficients are inter compared. A brief study of the stability of DMRT-QCA was also performed. Code for UMRT calculations for a single layer (either water or snow) were prepared and validated using energy conservation.

Ongoing work includes extending the above model to the case of multilayer stacks with refractive boundaries. For this extension the general DRTE solution and UMRT Jacobian formulation is being derived, programmed and validated. Comparison between the UMRT simulation and the field measurements obtained over Arctic sea ice is also being pursued.

VI. APPENDIX I: PROOF OF POSITIVE DEFINITE MATRICES

In order to apply the stable matrix inversion technique of DOTLRT, proof of the matrix $\overline{\overline{U}} + \overline{\overline{D}}$ being positive definite is as follows:

- 1) Separate the matrix $\overline{\overline{U}} + \overline{\overline{D}}$ into the sum of two matrices: one is a diagonal matrix, denoted as $\overline{\overline{S}}_d$ and the other is defined by $\overline{\overline{U}} + \overline{\overline{D}} - \overline{\overline{S}}_d$, denoted as $\overline{\overline{S}}_r$. The problem is now to prove the positive definiteness of both of these matrices. By design the matrix $\overline{\overline{S}}_d$ has elements:

$$\overline{\overline{S}}_d = \begin{bmatrix} \overline{\overline{S}}_{dv} & \overline{\overline{0}} \\ \overline{\overline{0}} & \overline{\overline{S}}_{dh} \end{bmatrix} \quad (62)$$

$$\left\{ \overline{\overline{S}}_{d\beta} \right\}_{ij} = \frac{k_{e\beta i} \delta_{ij}}{\mu_i} - \frac{\delta_{ij}}{\mu_i} \sum_{k=1}^M \gamma_k (P_{v\beta ki}^{++} + P_{v\beta ki}^{+-} + P_{h\beta ki}^{++} + P_{h\beta ki}^{+-}) \quad , \quad \beta = v \text{ or } h \quad (63)$$

Note that (63) is indeed the discretized form of $k_{e\beta} - k_{s\beta}$, which is always positive for passive media due to inevitable small losses.

2) From the above definition, the matrix $\overline{\overline{S}}_r$ is defined as

$$\overline{\overline{S}}_r = \begin{bmatrix} \underbrace{\overline{\overline{S}}_{rv}}_{2M \times M} & \underbrace{\overline{\overline{S}}_{rh}}_{2M \times M} \end{bmatrix} \quad (64)$$

$$\left\{ \overline{\overline{S}}_{r\beta} \right\}_{ij} = \frac{1}{\mu_i} \sum_{k=1}^M \gamma_k (P_{v\beta ki}^{++} + P_{v\beta ki}^{+-} + P_{h\beta ki}^{++} + P_{h\beta ki}^{+-}) \delta_{ij} - \sqrt{\frac{\gamma_i \gamma_j}{\mu_i \mu_j}} (P_{v\beta ij}^{++} + P_{v\beta ij}^{+-} + P_{h\beta ij}^{++} + P_{h\beta ij}^{+-}), \quad \beta = v \text{ or } h \quad (65)$$

Now consider the eigenvalues and eigenvectors of $\overline{\overline{S}}_r$, where $\overline{\overline{S}}_r \overline{\overline{u}} = \lambda \overline{\overline{u}}$. Following the development of Gershgorin's circle theorem the maximal value of the ratio $u_i / \sqrt{\mu_i \gamma_i}$ for all i is found

$$\left| \frac{u_{i_0}}{\sqrt{\mu_{i_0} \gamma_{i_0}}} \right| > \frac{u_i}{\sqrt{\mu_i \gamma_i}} \quad (66)$$

Assuming that $u_{i_0} > 0$ and noting that the phase matrix is symmetric, it follows that

$$\begin{aligned} \lambda u_{i_0} &= \frac{u_{i_0}}{\mu_{i_0}} \sum_{k=1}^M \gamma_k (P_{v\beta ki}^{++} + P_{v\beta ki}^{+-} + P_{h\beta ki}^{++} + P_{h\beta ki}^{+-}) \\ &\quad - \sqrt{\frac{\gamma_{i_0}}{\mu_{i_0}}} \sum_{j=1}^M \frac{u_j \gamma_j}{\sqrt{\mu_j \gamma_j}} (P_{v\beta ij}^{++} + P_{v\beta ij}^{+-} + P_{h\beta ij}^{++} + P_{h\beta ij}^{+-}) \\ &\geq \frac{u_{i_0}}{\mu_{i_0}} \sum_{k=1}^M \gamma_k (P_{v\beta ki}^{++} + P_{v\beta ki}^{+-} + P_{h\beta ki}^{++} + P_{h\beta ki}^{+-}) \\ &\quad - \sqrt{\frac{\gamma_{i_0}}{\mu_{i_0}}} \frac{u_{i_0}}{\sqrt{\mu_{i_0} \gamma_{i_0}}} \sum_{j=1}^M \gamma_j (P_{v\beta ij}^{++} + P_{v\beta ij}^{+-} + P_{h\beta ij}^{++} + P_{h\beta ij}^{+-}) \\ &= 0 \end{aligned}, \quad \beta = v \text{ or } h \quad (67)$$

3) A similar argument can be applied to the case of the matrix $\overline{\overline{U}} - \overline{\overline{D}}$. Hence, we conclude that both matrices $\overline{\overline{U}} + \overline{\overline{D}}$ and $\overline{\overline{U}} - \overline{\overline{D}}$ are symmetric and positive definite, and therefore applicable to the stable inversion technique used within DOTLRT.

VII. APPENDIX II: INHOMOGENEOUS SOLUTION TO A LINEAR TEMPERATURE PROFILE

Balancing (52), the terms with z dependency vanish, leading to

$$\begin{bmatrix} \overline{u}_1 \\ \overline{v}_1 \end{bmatrix} = \begin{bmatrix} \overline{\overline{U}} & \overline{\overline{D}} \\ \overline{\overline{D}} & \overline{\overline{U}} \end{bmatrix}^{-1} \begin{bmatrix} \overline{\gamma}_T \\ \overline{\gamma}_T \end{bmatrix} \quad (68)$$

To explicitly solve (68) we apply block matrix inversion [25] and obtain

$$\begin{aligned} & \begin{bmatrix} \bar{U} & \bar{D} \\ \bar{D} & \bar{U} \end{bmatrix}^{-1} \\ & = \begin{bmatrix} (\bar{U} - \bar{D}\bar{U}^{-1}\bar{D})^{-1} & -\bar{U}^{-1}\bar{D}(\bar{U} - \bar{D}\bar{U}^{-1}\bar{D})^{-1} \\ -\bar{U}^{-1}\bar{D}(\bar{U} - \bar{D}\bar{U}^{-1}\bar{D})^{-1} & (\bar{U} - \bar{D}\bar{U}^{-1}\bar{D})^{-1} \end{bmatrix} \end{aligned} \quad (69)$$

Applying (69) to (68) we have

$$\begin{bmatrix} \bar{u}_1 \\ \bar{v}_1 \end{bmatrix} = \begin{bmatrix} (\bar{I} - \bar{U}^{-1}\bar{D})(\bar{U} - \bar{D}\bar{U}^{-1}\bar{D})^{-1} \bar{\gamma}_T \\ (\bar{I} - \bar{U}^{-1}\bar{D})(\bar{U} - \bar{D}\bar{U}^{-1}\bar{D})^{-1} \bar{\gamma}_T \end{bmatrix} \quad (70)$$

The solution (70) can be simplified using the following derivation

$$\begin{aligned} & (\bar{U} + \bar{D}) \left[(\bar{I} - \bar{U}^{-1}\bar{D})(\bar{U} - \bar{D}\bar{U}^{-1}\bar{D})^{-1} \right] \\ & = (\bar{U} - \bar{D}\bar{U}^{-1}\bar{D})(\bar{U} - \bar{D}\bar{U}^{-1}\bar{D})^{-1} = \bar{I} \end{aligned} \quad (71)$$

$$\Rightarrow (\bar{I} - \bar{U}^{-1}\bar{D})(\bar{U} - \bar{D}\bar{U}^{-1}\bar{D})^{-1} = (\bar{U} + \bar{D})^{-1} = \bar{A}^{-1} \quad (72)$$

As a result of (71-72), (70) is, thus, equivalent as

$$\begin{bmatrix} \bar{u}_1 \\ \bar{v}_1 \end{bmatrix} = \begin{bmatrix} \bar{A}^{-1}\bar{F} \\ \bar{A}^{-1}\bar{F} \end{bmatrix} \quad (73)$$

Since $\bar{u}_1 = \bar{v}_1$ the remainder of (52) yields

$$\begin{aligned} & \begin{bmatrix} \bar{u}_o \\ \bar{v}_o \end{bmatrix} = \begin{bmatrix} \bar{U} & \bar{D} \\ \bar{D} & \bar{U} \end{bmatrix}^{-1} \begin{bmatrix} \bar{F}_o + \bar{u}_1 \\ \bar{F}_o - \bar{v}_1 \end{bmatrix} \\ & = \begin{bmatrix} \bar{A}^{-1}\bar{F}_o + (\bar{I} + \bar{U}^{-1}\bar{D})(\bar{U} - \bar{D}\bar{U}^{-1}\bar{D})^{-1} \bar{u}_1 \\ \bar{A}^{-1}\bar{F}_o - (\bar{I} + \bar{U}^{-1}\bar{D})(\bar{U} - \bar{D}\bar{U}^{-1}\bar{D})^{-1} \bar{v}_1 \end{bmatrix} \end{aligned} \quad (74)$$

Similarly, it can be shown that

$$(\bar{I} + \bar{U}^{-1}\bar{D})(\bar{U} - \bar{D}\bar{U}^{-1}\bar{D})^{-1} = (\bar{U} - \bar{D})^{-1} = \bar{B}^{-1} \quad (75)$$

Thus,

$$\begin{bmatrix} \bar{u}_o \\ \bar{v}_o \end{bmatrix} = \begin{bmatrix} \bar{A}^{-1} \bar{F}_o + \bar{B}^{-1} \bar{A}^{-1} \bar{\gamma}_T \\ \bar{A}^{-1} \bar{F}_o - \bar{B}^{-1} \bar{A}^{-1} \bar{\gamma}_T \end{bmatrix} \quad (76)$$

Finally, from (73,76), the inhomogeneous solution of (38) is

$$\begin{aligned} \begin{bmatrix} \bar{u}_{inh}(z) \\ \bar{v}_{inh}(z) \end{bmatrix} &= \begin{bmatrix} \bar{A}^{-1} \bar{F}_o + \bar{B}^{-1} \bar{A}^{-1} \bar{\gamma}_T - \bar{A}^{-1} \bar{\gamma}_T z \\ \bar{A}^{-1} \bar{F}_o - \bar{B}^{-1} \bar{A}^{-1} \bar{\gamma}_T - \bar{A}^{-1} \bar{\gamma}_T z \end{bmatrix} \\ &= \begin{bmatrix} \bar{A}^{-1} (\bar{F}_o - \bar{\gamma}_T z) + \bar{B}^{-1} \bar{A}^{-1} \bar{\gamma}_T \\ \bar{A}^{-1} (\bar{F}_o - \bar{\gamma}_T z) - \bar{B}^{-1} \bar{A}^{-1} \bar{\gamma}_T \end{bmatrix} \\ &= \begin{bmatrix} \bar{A}^{-1} \bar{F}(z) + \bar{B}^{-1} \bar{A}^{-1} \bar{\gamma}_T \\ \bar{A}^{-1} \bar{F}(z) - \bar{B}^{-1} \bar{A}^{-1} \bar{\gamma}_T \end{bmatrix} \end{aligned} \quad (77)$$

REFERENCES

- [1] A. G. Voronovich, A. J. Gasiewski, and B. L. Weber, "A fast multistream scattering-based jacobian for microwave radiance assimilation," *Geoscience and Remote Sensing, IEEE Transactions on*, vol. 42, pp. 1749–1761, Aug 2004.
- [2] M. A. Janssen, *Atmospheric Remote Sensing by Microwave Radiometry, Chapter 3*. Wiley, 1993.
- [3] A. J. Gasiewski, "Atmospheric temperature sounding and precipitation cell parameter estimation using passive 118-GHz O_2 observations," Ph.D. dissertation, Massachusetts Institute of Technology, 1988.
- [4] L. Tsang, J. A. Kong, and K. H. Ding, *Scattering of Electromagnetic Waves: Theories and Applications*. Wiley, 2000, vol. 1.
- [5] K. Stamnes and H. Dale, "A new look at the discrete ordinate method for radiative transfer calculation in anisotropically scattering atmospheres," *J. Atmos. Sci.*, vol. 38, pp. 387–399, 1981.
- [6] T. Nakajima and M. Tanaka, "Matrix formulations for the transfer of solar radiation in a plane-parallel atmosphere," *J. Quant. Spectrosc. Rad. Transf.*, vol. 35, pp. 13–21, 1986.
- [7] K. Stamnes, S. C. Tsay, W. Wiscombe, and K. Jayaweera, "Numerically stable algorithm for discrete ordinate method radiative transfer in multiple scattering and emitting layered media," *Appl. Opt.*, vol. 27, pp. 2502–2529, 1988.
- [8] L. Tsang, J. A. Kong, K. H. Ding, and C. O. Ao, *Scattering of Electromagnetic Waves: Numerical Simulations*. Wiley, 2000, vol. 2.
- [9] K. K. Tse, L. Tsang, C. H. Chan, K. H. Ding, and K. W. Leung, "Multiple scattering of waves by dense random distributions of sticky particles for applications in microwave scattering by terrestrial snow," *Radio Science*, vol. 42, pp. 1–14, Sep. 2007.
- [10] L. Tsang and J. A. Kong, *Scattering of Electromagnetic Waves: Advanced Topics*. Wiley, 2000, vol. 3.
- [11] L. Tsang, J. Pan, D. Liang, Z. Li, D. W. Cline, and Y. Tan, "Modeling active microwave remote sensing of snow using dense media radiative transfer (dmrt) theory with multiple-scattering effects," *Geoscience and Remote Sensing, IEEE Transactions on*, vol. 45, no. 4, pp. 990–1004, Apr. 2007.
- [12] E. Yakimiw, "Accurate computation of weights in classical gauss christoffel quadrature rules," *J. Comput. Phys.*, vol. 129, pp. 406–430, June 1996.
- [13] P. N. Swarztrauber, "On computing the points and weights for gauss legendre quadrature," *SIAM J. Sci. Comput.*, vol. 24, 2002.
- [14] A. Ishimaru, *Wave Propagation and Scattering in Random Media*. New York: Academic, 1978.
- [15] C. Matzler, *Thermal Microwave Radiation Applications for Remote Sensing, Chapter 3*. London: IET, 2006.

- 1
2 [16] S. Chandrasekhar, *Radiative Transfer*. New York: Dover, 1960.
3
4 [17] C. F. Bohren and D. R. Huffman, *Absorption and Scattering of Light by Small Particles*. Wiley, 1998.
5
6 [18] H. C. Van de Hulst, *Light Scattering by Small Particles*. Dover, 1957.
7
8 [19] S. G. Warren, "Optical constants of ice from the ultraviolet to the microwave," *Applied Optics*, vol. 23, pp. 1206–1225, 1983.
9
10 [20] R. S. Sekhon and R. C. Srivastava, "Snow size spectra and radar reflectivity," *J. Atm. Sci.*, vol. 27, pp. 299–307, Mar. 1970.
11
12 [21] J. S. Marshall and W. M. Palmer, "The distribution of raindrops with size," *J. Meteorol.*, vol. 5, pp. 165–166, Aug. 1948.
13
14 [22] T. Meissner and F. J. Wentz, "The complex dielectric constant of pure and sea water from microwave satellite observations," *Geoscience and Remote Sensing, IEEE Transactions on*, vol. 42, no. 9, pp. 1836–1849, Sep. 2004.
15
16 [23] S. Wolf and N. V. Voshchinnikov, "Mie scattering by ensembles of particles with very large size parameters," *Computer Physics Communications*, pp. 113–123, 2004.
17
18 [24] Y. Takano and K. N. Liou, "Phase matrix for light scattering by concentrically stratified spheres: Comparison of geometric optics and the exact theory," *Applied Optics*, vol. 49, no. 20, pp. 3990–3996, July 2010.
19
20 [25] Y. Choi and J. Cheong, "New expressions of 2x2 block matrix inversion and their application," *Automatic Control, IEEE Transactions on*, vol. 54, no. 11, pp. 2648–2653, Nov. 2009.
21
22 [26] M. Tian and A. J. Gasiewski, "Extended jacobian formulation of a unified microwave radiative transfer model: Numerical validation and field data intercomparison," *In Preparation*, 2012.
23
24
25
26
27
28
29
30
31
32
33
34
35
36
37
38
39
40
41
42
43
44
45
46
47
48
49
50
51



Miao Tian received the B.E. degree in electrical engineering from University of Electronic Science and Technology of China, Chengdu, China, in 2003 and the M.S.E.E degree in electrical engineering from University of Tulsa, Tulsa, OK, USA, in 2005. He is currently working toward the Ph.D. degree in the Department of Electrical, Computer, and Energy Engineering, University of Colorado, Boulder.

His current research interests include theoretical and numerical studies of passive and active radiative transfer modeling and retrieval algorithm in remote sensing and geoscience applications, remote sensing related electronic instrumentation, and other general microwave circuits and antenna design.

52
53
54
55
56
57
58
59
60



Albin J. Gasiewski (SM'81–M'88–SM'95–F'02) received the M.S. and B.S. degrees in electrical engineering and the B.S. degree in mathematics from Case Western Reserve University, Cleveland, OH, in 1983 and the Ph.D. degree in electrical engineering and computer science from the Massachusetts Institute of Technology, Cambridge, in 1989.

From 1989 to 1997, he was a Faculty Member with the School of Electrical and Computer Engineering, Georgia Institute of Technology, Atlanta, where he became an Associate Professor. He has developed and taught courses on electromagnetics, remote sensing, instrumentation, and wave propagation theory. From 1997 to 2005, he was with the U.S. National Oceanic and Atmospheric Administration's Environmental Technology Laboratory (ETL), Boulder, CO, where he was Chief of ETL's Microwave Systems Development Division. He is currently a Professor of electrical and computer engineering with the University of Colorado at Boulder (CU-Boulder) and Director of the CU-Boulder Center for Environmental Technology. His technical interests include passive and active remote sensing, radiative transfer, antennas and microwave circuits, electronic instrumentation, meteorology, and oceanography.

Prof. Gasiewski is past President (2004–2005) of the IEEE Geoscience and Remote Sensing Society (GRSS). He is a member of the American Meteorological Society, the American Geophysical Union, the International Union of Radio Scientists (URSI), Tau Beta Pi, and Sigma Xi. He currently serves as Vice Chair of U.S. National Committee/URSI Commission F. He served on the U.S. National Research Council's Committee on Radio Frequencies from 1989 to 1995. He was the General Cochair of the 2006 International Geoscience and Remote Sensing Symposium, Denver, CO, and a recipient of the 2006 Outstanding Service Award from the GRSS.

Peer Review